Applications of DINEOF to satellite-derived chlorophyll-a from a productive coastal region

by

Andrea Hilborn
B.Sc., University of Victoria, 2014

A Thesis Submitted in Partial Fulfillment
of the Requirements for the Degree of

MASTER OF SCIENCE

in the Department of Geography

Supervisory Committee

Applications of DINEOF to satellite-derived chlorophyll-a from a productive coastal region

by

Andrea Hilborn
B.Sc., University of Victoria, 2014

Supervisory Committee

Dr. Maycira Costa (Department of Geography)
Supervisor

Dr. Akash Sastri (Ocean Networks Canada)
Committee Member

Dr. David Atkinson (Department of Geography)
Committee Member

Abstract

Supervisory Committee
Dr. Maycira Costa (Department of Geography)
Supervisor
Dr. Akash Sastri (Ocean Networks Canada)
Committee Member
Dr. David Atkinson (Department of Geography)
Committee Member

A major limitation for remote sensing analyses of oceanographic variables is loss of spatial data. The Data INterpolating Empirical Orthogonal Functions (DINEOF) method has demonstrated effectiveness for filling spatial gaps in remote sensing datasets, making them more easily implemented in further applications. However, dataset reconstructions with this method are sensitive to the characteristics of the input data used. The spatial and temporal coverage of the input imagery can heavily impact the reconstruction outcome, and thus, further metrics derived from these datasets, such as phytoplankton bloom phenology. In this study, the DINEOF method was applied to a three-year time series of MODIS-Aqua chlorophyll-a of the Salish Sea, Canada. Spatial reconstructions were performed on an annual and multi-year basis at daily and week-composite time resolutions, and assessed relative to the original, clouded *chla* datasets and a set of extracted *in situ chla* measurements. A sensitivity test was performed to assess stability of the results with variation of cross-validation data and simulated scenarios of lower temporal data coverage. Daily input time series showed greater accuracy reconstructing *chla* (95.08-97.08% explained variance, $RMSE_{xval}$ 1.49 - 1.65 mg m^{-3}) than week-composite counterparts (68.99-76.88% explained variance, $RMSE_{xval}$ 1.87 – 2.07 mg m^{-3}), with longer time series of both types producing a better relationship to original *chla* pixel concentrations (R 0.95 over 0.94, RMSE 1.29 over 1.35 mg m^{-3}, slope 0.88 over 0.84). Original daily *chla* achieved a better relationship to *in situ* matchups than DINEOF gap-filled *chla,* with annual DINEOF-processed data performing better than the multi-year. The results of this study are of interest to those who require spatially continuous satellite-derived products, particularly from short time series, and encourage processing consistency in future DINEOF studies to allow unification for global purposes such as climate change studies (Mélin et al., 2017).

Table of Contents

List of Tables

List of Figures

List of Symbols

Symbol	Name	Units
α	fixed water reflectance ratio	
$chla$	chlorophyll-a concentration	mg m^{-3}
$chla_{insitu}$	extracted *in situ chla* samples	mg m^{-3}
$chla_{rec}$	DINEOF-reconstructed *chla*	mg m^{-3}
$chla_{rec\text{-}o}$	*chla* reconstructed in location of $chla_{sat}$ pixel	mg m^{-3}
$chla_{rec\text{-}r}$	*chla* reconstructed in location of missing data	mg m^{-3}
$chla_{sat}$	satellite *chla,* calculated by OC3M algorithm	mg m^{-3}
$chla_{sat+rec}$	satellite *chla* with gaps filled with DINEOF-reconstructed *chla*	mg m^{-3}
$chla_{xval}$	satellite *chla* for cross-validation with DINEOF	mg m^{-3}
$D1$	DINEOF applied to one-year period of daily $chla_{sat}$	
$D3$	DINEOF applied to three-year period of daily $chla_{sat}$	
ε	aerosol reflectance ratio	
γ	sensor-solar transmittance ratio	
ρ_a	aerosol reflectance	
R	coefficient of correlation	
R^2	coefficient of determination	
$RMSE$	root mean square error	mg m^{-3}
$RMSE_{xval}$	root mean square error of cross-validation pixels	mg m^{-3}
σ	standard deviation of sample	mg m^{-3}
SST	sea surface temperature	^{o} C
TSM	total suspended matter	mg l^{-1}
$W1$	DINEOF applied to one-year period of week-composite $chla_{sat}$	
$W3$	DINEOF applied to three-year period of week-composite $chla_{sat}$	
$\bar{X}$	mean of sample	mg m^{-3}
$\bar{X}_{filt}$	filtered mean of sample	mg m^{-3}

Acknowledgments

First of all, thank you to Dr. Maycira Costa, my supervisor. Your guidance and motivation over the course of this project and total passion for this field has translated into much more than completion of my master's thesis. Thanks as well to my committee, Dr. Akash Sastri and Dr. David Atkinson, for being knowledgeable resources throughout, and to Dr. Emmanuel Devred for the thorough comments on this thesis.

Without my partner, Jeremy Krogh, I would not be here. Thank you so much for your support, intelligence and patience throughout the past few years and more. Thank you as well to my family; you help me prioritize what is important (tea) and keep the witticisms flowing. In particular, thanks to my dad, for infecting my life with maps long before I found geomatics.

Thank you so much to the amazing friends and colleagues I have been lucky enough to know and meet during the past few years, particularly the members of the SPECTRAL Lab and Geography Department, including Sarak, Karyn, Stephen, Fernanda, Camila, Natasha, Nicole, Sasha, Kyle, Pei-Ling, and more. You have been so willing to go out of your way to offer support, knowledge, puns and beyond. I am also appreciative to the incredible ocean-colour community I was lucky enough to meet, who have inspired me and strengthened my abdominal muscles with laughter at the same time; Quinten, Carina, Charlotte, Juancho, and Liesbeth, to name a few of you.

This project would not have been possible without the GHER group for openly providing DINEOF, the NASA OBPG for hosting the data and software used, and DFO/IOS for providing the *in situ* samples. Additionally, I am extremely thankful to the IOCCG for hosting the Summer Lecture Series; attending was a life-changing experience and it is a huge service to the field of ocean optics. Funding for this project was generously provided by the Pacific Salmon Foundation, Mitacs and MEOPAR.

1. Introduction

Advancements in remote sensing technology, including increased frequency of data acquisition and rapid developments in algorithms and computational processing, continue to improve ocean observation and monitoring capabilities (Blondeau-Patissier, Gower, Dekker, Phinn, & Brando, 2014; Sathyendranath, Brewin, Jackson, Mélin, & Platt, 2017). However, satellite-based spatial and temporal monitoring of oceanic biogeochemical variables, such as chlorophyll-a concentration (*chla*), which depend on the ability to measure water reflectance, is still a challenge. Among several reasons, obstacles include clouds obscuring measurements of ocean reflectance and difficulties removing atmospheric signal, in addition to the contaminating effects of sun-glint, adjacency from land and bottom-reflectance (Sirjacobs et al., 2011). Simple and commonly implemented strategies for mitigating low spatial coverage of satellite image time series are to condense information temporally (e.g., minimize spatial gaps by using composite scenes), or reduce spatial resolution (Antoine et al., 2004). Other methods for gaining data coverage consist of multi-mission merging (Gregg et al., 2007; Kahru, Kudela, Manzano-Sarabia, & Greg Mitchell, 2012) or interpolation, which includes optimal interpolation (OI) (Bennett, 2002), construction of data based on pixel neighbourhoods (Casey, Arnone, & Flynn, 2007), utilization of differing spatial scales (P. E. Land, Shutler, Platt, & Racault, 2014), kriging (Müller, 2007; Sherwood, 2000), Lagrangian approaches (Jönsson & Salisbury, 2016), and empirical orthogonal function (EOF) methods (Smith, Reynolds, Levezey, & Stokes, 1996; Taylor, Losch, Wenzel, & Schröter, 2013).

Among EOF interpolation methods, the Data INterpolating Empirical Orthogonal Functions (DINEOF) technique (A. Alvera-Azcárate, Barth, Rixen, & Beckers, 2005; Beckers & Rixen, 2003) has demonstrated superior results relative to other methods at diverse levels of cloud coverage (Taylor et al., 2013). Recent DINEOF applications include spatial reconstructions of satellite-derived time series of sea surface temperature (SST) (Beckers, Barth, & Alvera-Azcárate, 2006; Ganzedo, Alvera-Azcárate, Esnaola, Ezcurra, & Sáenz, 2011; Y. Li & He, 2014; Sirjacobs et al., 2011), sea surface salinity (SSS) (Aida Alvera-Azcárate, Barth, Parard, & Beckers, 2016), *chla* (Corredor-Acosta, Morales, Hormazabal, Andrade, & Correa-Ramirez, 2015; Waite & Mueter, 2013), turbidity (Aida Alvera-Azcárate, Vanhellemont, Ruddick, Barth, & Beckers, 2015), total suspended matter (TSM) (Nechad, Alvera-Azcárate, Ruddick, & Greenwood, 2011), and photosynthetically available radiation (PAR) (McGinty, Guðmundsson, Ágústsdóttir, & Marteinsdóttir, 2016). DINEOF is also used in multivariate form, exploiting natural correlations between variables including SST+*chla* (Miles, He, & Li, 2009) or SST+*chla*+wind fields (Alvera-Azcárate, Barth, Beckers, & Weisberg, 2007). Existing implementations of DINEOF utilize input data at different time scales, for instance, varied study periods and time resolutions (e.g., from less than one year to more than a decade using daily or week-composite imagery) for different oceanographic regions, such as open ocean and coastal waters. Some studies have considered the impact of input dataset time resolution on the results as it impacts the ability of DINEOF to capture regional oceanographic features. However, studies rarely present the DINEOF accuracy according to differing time scales of the input data, applying it to datasets for further analyses without providing reconstruction statistics. As a result, there is a need to further

examine variation of DINEOF implementations in greater detail considering that DINEOF is often the precursor to further uses of a given dataset, and uncertainties are already present in satellite-derived biogeochemical time series (Land et al., 2018).

In this study, DINEOF was applied to daily and week-composite satellite-derived *chla* to examine the length of input time series on the accuracy of the reconstructed results. Specifically, a comparison of DINEOF implementations is presented here, to fill data gaps of a three-year chlorophyll-a time series for the Salish Sea, located on the west coast of British Columbia, Canada. *Chla* derived from the Moderate Resolution Imaging Spectroradiometer on satellite Aqua (MODISA) were reconstructed in two commonly used image formats, daily and week-composite, to evaluate the accuracy of the DINEOF products. Additionally, DINEOF implementations considered differing time resolutions, where annual constraints were applied to the dataset in addition to interpolating the datasets in entirety, to examine the effects of lengthy winter gaps and inconsistent annual dynamics of phytoplankton phenology present in the study region. A sensitivity test examined the impact of varied cross-validation data required for DINEOF and dataset length on the reconstruction accuracy. Further, a dataset of extracted *in situ chla* samples was accessed for comparison between original and reconstructed satellite *chla*. The resulting DINEOF approach allows production of *chla* fields more effective for studying long-term trends and addressing broader ecological questions for this region, including further investigations of bottom-up effects of phytoplankton phenology on higher trophic levels (Masson & Perry, 2013). As a Case II water body with low annual satellite data availability due to cloud coverage and low sun angle during the winter months, DINEOF

implementations and evaluations of the Salish Sea are applicable to other regions with similar constraints.

2. Materials and Methods

2.1. Study Area

The Salish Sea is a semi-enclosed coastal sea adjacent to the province of British Columbia, Canada, and Washington State, USA. The region encompasses the Strait of Georgia (SoG), Juan de Fuca Strait (JFS), and Puget Sound (PS) over an area of approximately 18,000 km^2 (Figure 1). The Fraser River is the dominant source of fresh water, dissolved organic matter, and particulate matter, contributing approximately 158 x 109 m^3 yr^{-1} of water and 19 x 109 kg yr^{-1} of sediment directly into the Strait of Georgia (Allen & Wolfe, 2013; Johannessen, Macdonald, & Paton, 2003). The annual discharge is snowmelt-dominated, increasing by up to seven times during the spring freshet with its peak typically in June (Masson, 2006). Fraser River discharge drives an estuarine complex in the southern Salish Sea, where fresher surface waters are carried from the south SoG through the JFS to the Pacific Ocean and nutrient-rich deep-ocean water is exchanged (Mackas & Harrison, 1997). Although circulation also occurs through northern passages, modelling studies show that the JFS accounts for nearly 20 times greater flow (Khangaonkar, Long, & Xu, 2017). Queen Charlotte Strait (QCS), to the north of the SoG via Johnstone Strait, is included in this study considering its use in salmon migration research (Porter, Rechisky, Winchell, & Welch, 2016).

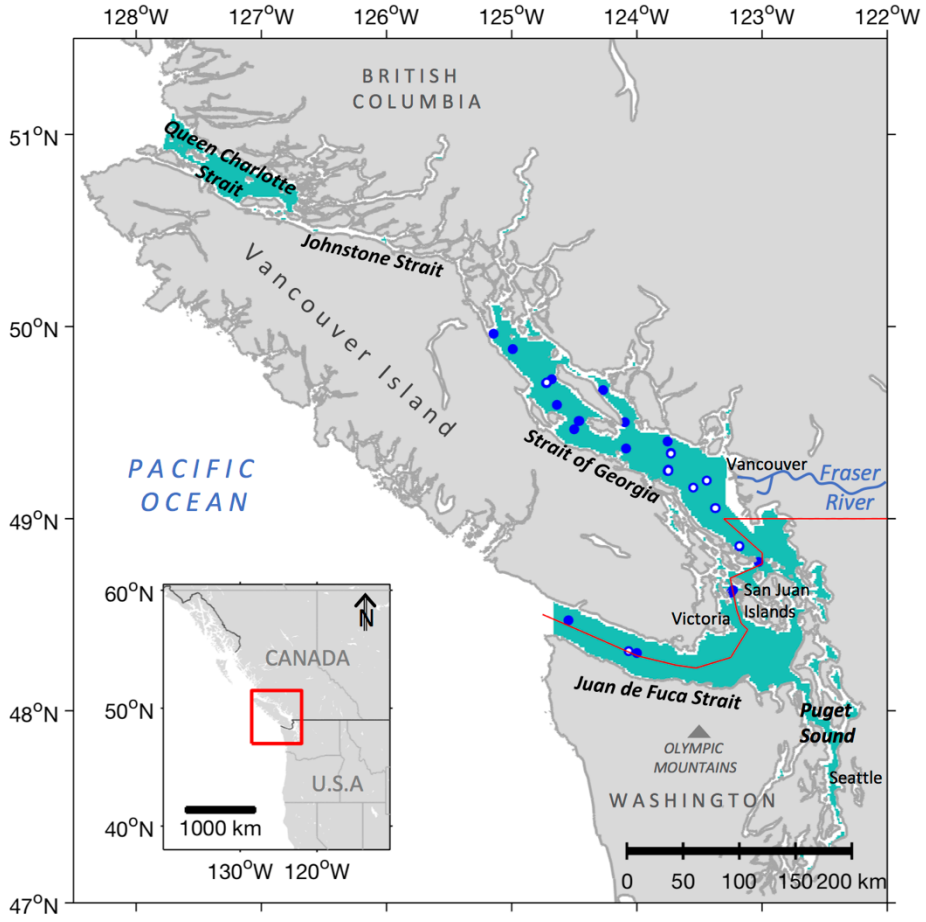

Figure 1. The Salish Sea, oceanic and geographic features, and population centres. The region includes the Juan de Fuca Strait (JFS), Strait of Georgia (SoG), Puget Sound (PS), and Queen Charlotte Strait (QCS). Locations of *in situ chla* matchups (section 2.4.2) indicated by blue (DINEOF-reconstructed *chla*) and blue-ringed circles (satellite and DINEOF-reconstructed *chla*).

The Salish Sea is one of the most productive regions of the northeast Pacific Ocean (Harrison, Fulton, Taylor, & Parsons, 1983; Jackson, Thomson, Brown, Willis, & Borstad, 2015; Masson & Peña, 2009) and sustains large biodiversity (Ware & Thomson, 2005), including being an important migration region for multiple species of Pacific salmon (Chittenden, Beamish, & McKinley, 2009). Phytoplankton productivity varies markedly temporally and spatially, due to physical forcings, which include Fraser River

discharge, tidal activity, solar radiation, and wind stress (Allen & Wolfe, 2013; Collins, Allen, & Pawlowicz, 2009; Masson & Peña, 2009; Yin et al., 1997). For the SoG, *chla* ranges from less than 1.00 mg m^{-3} in winter months to approximately 40.00 mg m^{-3} during spring bloom conditions (Harrison et al., 1983; M. Li, Gargett, & Denman, 2000; Peña, Masson, & Callendar, 2016). Here, seasonal phytoplankton blooms are linked to water density stratification combined with increased solar radiation in springtime, with weaker bloom events occurring in the fall (Allen & Wolfe, 2013; Carswell et al., 2017; Collins et al., 2009; Jackson et al., 2015; Masson & Peña, 2009), a pattern similarly observed in QCS (Jackson et al., 2015; Perry, 1984). In the JFS, on the other hand, *chla* concentrations consistently remain low regardless of the high nutrient availability sustained by mixing and deep exchange of Pacific Ocean waters, as the surface waters are less stratified than the SoG (Mackas, Louttit, & Austin, 1980; Mackas & Harrison, 1997).

Optically, the Salish Sea is defined as a dynamic Case II water body, in which the optical properties of surface waters are heavily influenced by suspended matter concentrations and dissolved organic matter (Loos & Costa, 2010; Loos, Costa, & Johannessen, 2017; Phillips & Costa, 2017). Attenuation in estuarine waters of the Fraser River plume is influenced by colour dissolved organic matter (CDOM) absorption and inorganic suspended matter scattering. Absorption from CDOM and *chla* makes up a higher component of total attenuation in waters north of the Fraser River plume, relative to the rest of the study area (Loos & Costa, 2010; Phillips & Costa, 2017).

2.2. Data Sets

Three years (2014-2016) of MODISA imagery were processed from level 1A (L1A) to level 3 (L3) OC3M *chla* products using the MUMM-SWIR atmospheric

correction approach based on (Carswell et al., 2017). L3 time series at both daily and week-composite temporal resolutions were produced. A set of extracted in situ *chla* (referred to as $chla_{insitu}$) was accessed for comparison with the satellite-derived *chla* (referred to as the 'original' dataset, or $chla_{sat}$) and reconstructed *chla* fields.

2.2.1. Satellite *chla* time series

MODISA L1A images were acquired from the NASA Ocean Biology Processing Group (OBPG) ("NASA Ocean Color," n.d.) bounding 47.0 - 51.0° N and 122.5 - 128.0° W. Imagery were processed at ~1 km^2 resolution using the SeaWiFS Data Analysis Software (SeaDAS) version 7.3 ("NASA SeaDAS," n.d.) and MATLAB. Winter scenes (November 25th - February 18th) were excluded due to low solar elevation conditions (Carswell et al., 2017; McGinty et al., 2016). L1A imagery were first corrected for atmospheric effects using the SWIR-MUMM atmospheric correction approach (Carswell et al., 2017; Komick, 2007). This approach initially retrieves mean aerosol reflectance (ρ_a), sensor diffuse transmittance and solar diffuse transmittance at 748/869 nm over clear waters of the central SoG from SWIR-corrected imagery based on (Wang, 2007). The NIR aerosol single-scattering ratio (ε) and sensor-solar transmittance ratio (γ) were identified for each scene and used with the MUMM atmospheric correction to reprocess the L1A time series, using the standard NIR water-leaving reflectance ratio (α) for moderately turbid waters of 1.945 (Ruddick, Ovidio, & Rijkeboer, 2000). Following retrieval of atmospherically corrected remote sensing reflectance, $chla_{sat}$ concentrations were calculated using the OC3M algorithm (O'Reilly et al., 2000). In recent studies of the Salish Sea, R values of 0.74 (RMSE 2.14 mg m^{-3}) (Carswell et al., 2017) and 0.85 (RMSE 2.63 mg m^{-3}) (Komick, 2007) have been achieved for SWIR-MUMM corrected

OC3M-derived *chla*, which represent improved results compared to other *chla* algorithms and atmospheric correction methods tested for the region (Carswell et al., 2017; Komick, Costa, & Gower, 2009).

Several flags were subsequently applied to the $chla_{sat}$ for quality-control purposes. The standard flag for removing straylight-contaminated pixels was altered from using a 5x7 (Meister, Zong, & McClain, 2008) to a 3x3 window to retain a larger number of $chla_{sat}$ pixels. This window size still captures ~99.6% of the high-radiance point-spread function (PSF) in VIS/NIR bands (Meister & McClain, 2010). Further, pixels higher than 40.00 mg m^{-3} are not typical even during bloom conditions in this region (Carswell et al., 2017; Jackson et al., 2015), and were therefore removed, amounting to 1.73% of total pixels. Aside, NASA standard quality flags were applied during image processing (e.g., (Kahru et al., 2012; "NASA Ocean Color," n.d.)). Finally, a week-composite time series was created from binning the quality-controlled L2 daily $chla_{sat}$ products into 8-day 'weeks', and both the daily and week-composite imagery were mapped to a ~1km^2 equal-area grid using area-weighting to reduce distortion artifacts ("NASA Ocean Color," n.d.) and masked to constrain pixels to the Salish Sea region (Figure 1).

The two resulting datasets consisted of 540 daily $chla_{sat}$ scenes, of a potential 837, and 105 week-composite $chla_{sat}$ scenes, of a potential 138 scenes (Figure 2, Table 1; for Table 1 see section 2.3.2). These datasets show that the greatest number of available $chla_{sat}$ scenes per year occurred in August of 2014 and 2016, and May of 2015 (Figure 2a). By month, spatial coverage of Salish Sea $chla_{sat}$ for the daily and week-composite time series ranged from 10.0 - 40.0% and 40.0 - 90.0%, respectively (Figure 2b). Though the monthly coverage of the daily time series is on average 30% lower than the week-

composite monthly coverage, the temporal pattern is very similar, showing lower spatial coverage in February and March, followed by an increase to maximum in September. Excluding the winter months, the mean gap between consecutive scenes (e.g., scenes with zero coverage removed) of the daily time series was 2 days and the longest was 12 days. The week-composite datasets only experienced one gap of one week between consecutive scenes due to the reduction of temporal dimension, though some scenes had very low spatial coverage.

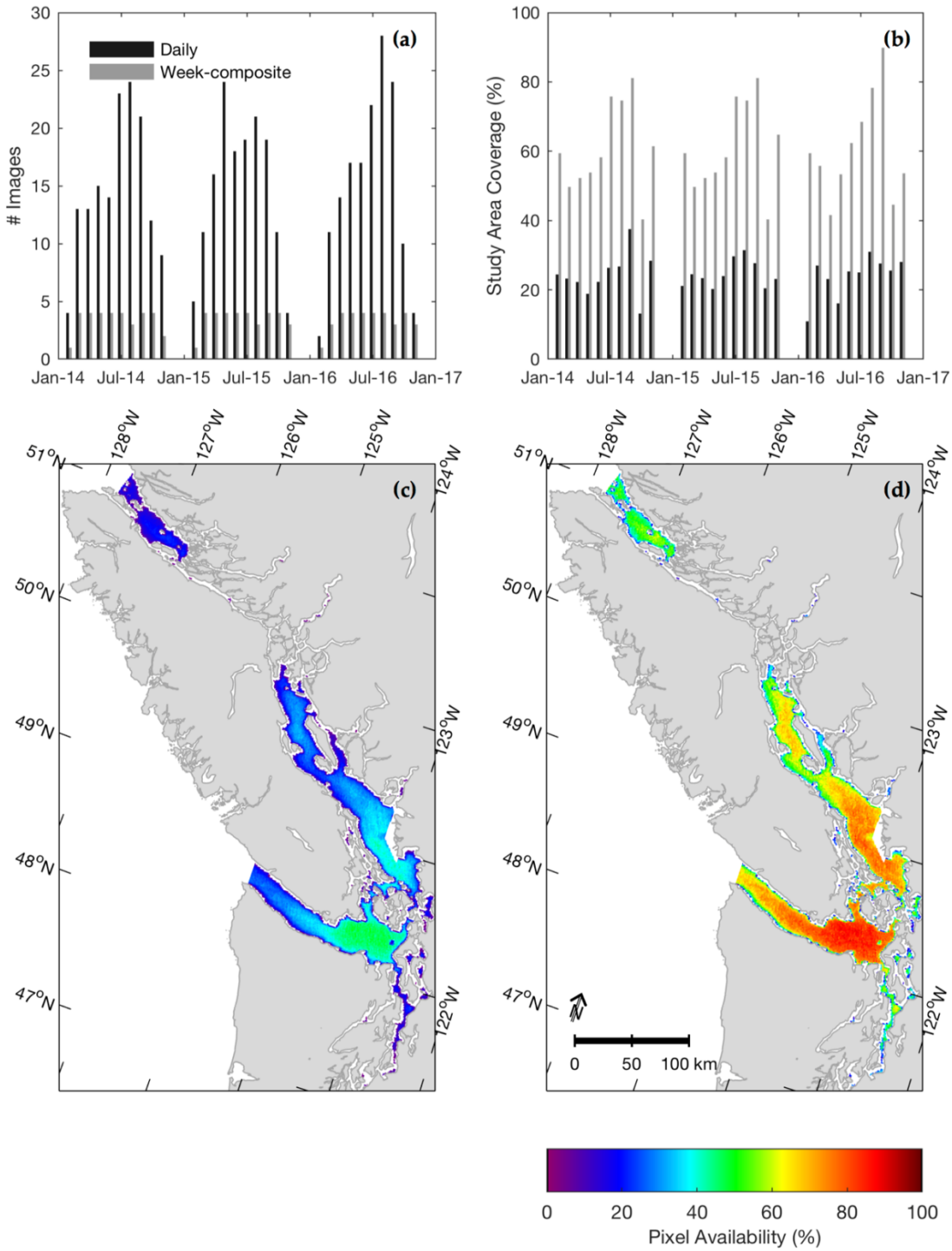

Figure 2. Temporal coverage displayed as (a) number of images per month and (b) percent spatial coverage for each month. February and November data coverage is limited due to the seasonal cutoffs from low solar elevation angle. For both filtered image datasets (445 daily scenes and 105 week-composite scenes, Table 1), spatio-temporal pixel coverage is demonstrated as percent occurrence of each pixel in the image time series. These (c) daily and (d) week-composite figures reflect the

greater coverage achieved through use of $chla_{sat}$ composites.

For daily $chla_{sat}$, the presence of a given pixel, expressed as percentage of the available image time series, was 27 ± 12% (Figure 2c), while the week-composite $chla_{sat}$ pixels were present 64 ± 18% of the dataset (Figure 2d). For both daily and week-composite $chla_{sat}$, the lowest per-pixel coverage occurred nearest the coast and in narrower straits and fjords, particularly in the QCS, north SoG and PS regions. The highest coverage occurred in the east JFS region south of the San Juan Islands, corresponding to the prominent rain shadow on the lee side of the Olympic Mountains (Mass, Johnson, Warner, & Vargas, 2015).

2.2.2. *In situ* dataset

A dataset of extracted $chla_{insitu}$ surface samples (depth ≤ 5m) spanning March, 2014 to November, 2016 (n = 374) was accessed from the Department of Fisheries and Oceans Canada data archive from the Institute of Ocean Sciences (Fisheries and Oceans Canada, Pacific Region, n.d.). Sample processing corresponded to filtration onto 25 mm GF/F filters, extraction in 90% acetone and analysis with a Turner 10AU fluorometer (Barwell-Clarke & Whitney, 1996; Holm-Hansen, Lorenzen, Holmes, & Strickland, 1965). The majority of samples were from the Strait of Georgia & Strait of Juan de Fuca Water Properties Survey. Samples were located throughout the entire study region with the majority located in the Strait of Georgia and at repeated stations near the Fraser River plume, and concentrations ranging from 0.29 - 36.00 mg m^{-3}, representing the dynamic range of the study region. *In situ* samples were screened for matchups with daily $chla_{sat}$ to within ± 3 hours of image acquisition.

2.3. DINEOF

This section presents a brief description of the DINEOF method and its framework for implementation in this study. This is followed by the details of the $chla_{sat}$ time series pre-processing before input to DINEOF. DINEOF was implemented using the 3.0 Linux binary available through the University of Liège GeoHydrodynamics and Environment Research group (GHER) (Alvera-Azcárate, Barth, Sirjacobs, Lenartz, & Beckers, 2011; "DINEOF - GHER," n.d.); MATLAB was used to prepare data for reconstruction and analysis.

2.3.1. Description and implementation

As part of the DINEOF implementation, a dataset of satellite imagery is decomposed spatially and temporally by iterative sequential calculations of the dominant spatial and temporal EOFs and accompanying singular values; with this information, any point in a matrix can be estimated. This method is sensitive to the number of images in a time series, the total amount of missing data, and the values of the pixels themselves (Alvera-Azcárate et al., 2005).

Prior to DINEOF, the mean of the input dataset is removed, missing values are set to zero, and an independent cross-validation dataset (~1 - 3% of the original valid satellite pixels (Alvera-Azcárate et al., 2005)) is identified and removed from the input dataset. Operationally, input images are arranged as a 2-dimensional spatial-temporal field, with one scene per row. Sequential EOF modes are then calculated iteratively using a singular value decomposition technique, beginning with the first mode. Throughout the procedure the cross-validation pixels are utilized to calculate accuracy between the original pixel values and corresponding DINEOF-calculated values. Once convergence of

cross-validation data is reached for an EOF mode, calculation of the following mode commences. The optimal number of EOFs for reconstructing the dataset is identified when the minimum RMSE of cross-validation pixels ($RMSE_{xval}$) is reached (Beckers & Rixen, 2003). Once this optimized number of EOFs is identified, the cross-validation pixels are returned to the matrix and the process is repeated. The final product is a set of spatial and temporal EOF modes and corresponding singular values which are linearly combined to produce a reconstructed field.

Here, I investigated the outcomes of varying the form of the input data used (i.e. daily or week-composite scenes) and time series length (annual or three consecutive years) on DINEOF reconstruction accuracy for a relatively small-scale dynamic region. The following framework was applied to each time series:

1. Reconstruction of *chla* spanning three years, 2014 - 2016, using the maximum amount of data available for the time period, where reconstructions with daily and week-composite data are referred to as D3 and W3, respectively; and
2. Reconstruction of *chla* products on an annual basis (2014, 2015, 2016) in order to constrain variability and reduce influence of lengthy gaps during the winter months. These are referred to as D1 ($D1_{2014}$, $D1_{2015}$, $D1_{2016}$) and W1 ($W1_{2014}$, $W1_{2015}$, $W1_{2016}$) reconstructions, considering daily and week-composite data respectively.

2.3.2. Pre-processing

Prior to DINEOF, all $chla_{sat}$ were $\log_{10}$ transformed to normalize the distribution (Campbell, 1995); as such, subsequent discussion refers to $\log_{10}$ mg m^{-3} unless otherwise stated. Additionally, each input time series was screened for quality by removing any scenes with less than 2% sea coverage, likely representing erroneous data (Alvera-

Azcárate et al., 2015; Li & He, 2014; Nechad et al., 2011); spatial distribution of the input data was not considered in this analysis.

The following information was then specified for each input dataset:

1. A mask identifying acceptable pixels to be reconstructed. Mask layers were defined to distinguish land from sea pixels, and to exclude individual ocean pixels present in less than 2% of the $chla_{sat}$ scenes. Finally, for consistency, the masks were unified to identify valid sea pixels common to all input datasets.
2. $chla_{sat}$ pixels to be used for cross-validation ($chla_{xval}$). $chla_{xval}$ pixels were identified randomly throughout each input dataset. For consistency between reconstructions of the same form (e.g., daily or week-composite), cross-validation data were identified for each year individually and concatenated for use with the corresponding three-year reconstruction.
3. A temporal ID of each $chla_{sat}$ image in the time series. The time increment of each $chla_{sat}$ image was specified by using day number as time-step for D1 and D3, and week number for W1 and W3.

During processing, the temporal covariance matrix was filtered, which improves reconstruction results by reducing inconsistencies calculated in the temporal EOF modes (Alvera-Azcárate, Barth, Sirjacobs, & Beckers, 2009). In our study, filtering signals shorter than one time increment was found to be optimal. Finally, when reconstructing datasets with DINEOF, both an entirely reconstructed field and field of $chla_{sat}$ where gaps are filled using the reconstructed data are possible. Both were utilized during this analysis, referred to as 'reconstructed' ($chla_{rec}$) and 'gap-filled' *chla* ($chla_{sat+rec}$),

respectively. Of the entirely reconstructed images, $chla_{rec}$ pixels replacing an original $chla_{sat}$ pixel are referred to as $chla_{rec\text{-}o}$, and $chla_{rec\text{-}r}$ when representing new data.

Table 1. Input data characteristics of each trial. The initial number of processed $chla_{sat}$ scenes is contrasted with scenes remaining after DINEOF pre-processing. Across trials, each input image could contain up to a maximum of 13 846 pixels. The missing data of each input dataset is shown as pixels missing, total number of $chla_{sat}$ pixels, and percent missing data.

	Period (year)	N scenes (before 2% filter)	N scenes (after 2% filter)	Pixels missing (Total pixels)[1]	Missing data (%)
$D1_{2014}$	2014	185	148	15.32 (20.49)	74.77
$D1_{2015}$	2015	168	148	15.57 (20.49)	75.99
$D1_{2016}$	2016	187	149	14.78 (20.6)	71.65
D3	2014 - 2016	540	445	45.67 (61.61)	74.13
$W1_{2014}$	2014	35	34	1.87 (4.71)	39.67
$W1_{2015}$	2015	35	35	2.10 (4.85)	43.36
$W1_{2016}$	2016	35	34	1.78 (4.71)	37.82
W3	2014 - 2016	105	103	5.75 (14.26)	40.31

[1] Values are x 10^5

2.4. Evaluation of reconstructions

Reconstruction success was assessed based on global statistics between $chla_{sat}$ and $chla_{rec\text{-}o}$ pixel values. The sensitivity of each outcome to variations in cross-validation data points and number of input scenes was investigated by repeating DINEOF with subsets of each input dataset. Finally, the daily DINEOF-derived $chla_{sat+rec}$ were evaluated against available $chla_{insitu}$ to characterize the overall accuracy of the daily reconstructions.

2.4.1. Reconstruction effectiveness and comparison to $chla_{sat}$

Reconstructions were assessed based on the number of optimal EOFs calculated, the proportion of input dataset variance captured, and the $RMSE_{xval}$ achieved (Wilks, 2006). Further, the accuracy of all $chla_{rec\text{-}o}$ to $chla_{sat}$ pixels was evaluated based on the RMSE (Equation (1)), accounting for the number degrees of freedom, slope, intercept, and squared Pearson correlation coefficient (R) (Equation (2)) retrieved at each time resolution (Mauri, Poulain, & Južnič-Zonta, 2007). To compare $chla_{sat}$ and $chla_{rec\text{-}o}$ annually, these statistics were retrieved for each year separately from the multi-year reconstructions (referred to as $D3_{2014}$, $D3_{2015}$ and $D3_{2016}$; $W3_{2014}$, $W3_{2015}$ and $W3_{2016}$).

$$RMSE = \sqrt{\frac{1}{n-2}\sum_{k=1}^{n}(r_k - s_k)^2} \quad (1)$$

$$R = \frac{\sum_{k=1}^{n}(s-\bar{s})(r_k-\bar{r})}{\sqrt{\sum_{k=1}^{n}((s_k-\bar{s})^2)(\sum_{k=1}^{n}(r_k-\bar{r})^2}} \quad (2)$$

where n is the number of samples, s is the $chla_{sat}$ pixel value and r is the corresponding $chla_{rec\text{-}o}$ pixel.

The coefficient of determination (R^2) between $chla_{sat}$ and $chla_{rec\text{-}o}$ was retrieved for each grid point through the three-year time series for each reconstruction method (Brewin et al., 2014). The p-value corresponding to each R^2 pixel was calculated for a measure of significance, where R^2 pixels with a p-value > 0.05 were removed from consideration. For this analysis, the annual reconstructions (D1, W1) were concatenated to form three-year time series to increase the number of samples for each pixel.

Further, a sensitivity test was performed to investigate the stability of the results with respect to the selected $chla_{xval}$ pixels and length of the input dataset. To conduct this test, between 10 - 90% of the input scenes for each $chla_{sat}$ dataset were removed and processed with DINEOF. This was repeated 30 times for each dataset size, where the corresponding cross-validation points, masks and time increment information required for input were generated separately for each (following section 2.3.2). The reconstruction $RMSE_{xval}$, number of EOFs produced and percent of missing data were used to assess stability of the reconstructions. The mean, minimum, maximum, and first/third quartiles were examined for the resulting $RMSE_{xval}$ at each dataset size to assess normality of the repeated results.

2.4.2. *In situ* comparison

Satellite *chla* matchup data were extracted from $chla_{sat}$, and D1 and D3 $chla_{sat+rec}$ via the filtered mean ($\bar{X}_{filt}$) (Equation (3)) of a 3x3 window at the *in situ* location, provided a minimum of 5 pixels of this window were available and the coefficient of variation was below 0.2 (Bailey & Werdell, 2006). Week-composite $chla_{sat+rec}$ scenes were not used for comparison with $chla_{insitu}$.

$$\bar{X}_{filt} = \frac{\sum_{k=1}^{n}(1.5\sigma - \bar{X}) < X_k < (1.5\sigma + \bar{X})}{N} \quad (3)$$

n is the original number of pixels, *N* is the number of values within the specified range, $\bar{X}$ is the unfiltered mean, X_k is a given *chla* pixel, and σ is the standard deviation of the window before filtering. Of 374 *in situ* samples collected over the three-year period, 3.5% (n=13) were retained for comparison with the original $chla_{sat}$ and 12.0% (n=45) to the $chla_{sat+rec}$. The majority of these matchups occurred in July for $chla_{sat}$, and June, July and September (n=31) for $chla_{sat+rec}$. Figure 1 illustrates the location of these matchup samples in the Salish Sea. Slope, intercept, and R were retrieved, and RMSE was calculated as a measure of accuracy (Werdell et al., 2009). Due to the low number of matchups, the three D1 years (2014 - 2016) were combined. Further, the $chla_{rec\text{-}r}$ data were not used in this evaluation, as retaining original satellite $chla_{sat}$ values is desired for the final, spatially continuous images of the region.

3. Results

3.1. DINEOF Reconstruction Statistics

The results of multiple implementations of DINEOF demonstrated higher performance (lower $RMSE_{xval}$, a greater number of calculated EOFs, and higher

explained variance for all input datasets) reconstructing daily $chla_{sat}$ rather than week-composite (Table 2), and reconstructing datasets with greater number of input scenes (Table 1). Specifically, the achieved $RMSE_{xval}$ for the daily reconstructions exhibited values ranging from 1.49 – 1.65 mg m^{-3}, capturing 95.08 – 96.33% of the $chla_{sat}$ variance with between 9 and 11 EOFs for individual years (D1), while 97.08% with 26 EOFs for the multi-year dataset (D3) (Appendix A). Further, the daily reconstructions exhibited the highest pixel density along the 1:1 line (Figure 3a, 3c) due to the improved results and greater number of pixels than week-composite datasets. Week-composite reconstructions demonstrated slightly higher $RMSE_{xval}$ (1.87 – 2.07 mg m^{-3}), with 68.99% of the $chla_{sat}$ variance captured with three EOFs for yearly input data (W1) to 76.88% with 8 EOFs for multi-years (W3). Week-composite reconstructions demonstrated a greater spread of $chla_{sat}$ and $chla_{rec\text{-}o}$ values and poorer linear relationship (Figure 3b, 3d). However, it is evident that the distribution of $chla_{sat}$ concentrations for this study played a role in the reconstruction outcomes (Figure 3), as $chla_{rec\text{-}o}$ were under-estimated at higher concentrations (> 20.00 mg m^{-3}). For both daily and week-composite reconstructions, the three-year input data time series produced better global results than the annual counterparts. However, the global accuracy of results for each form of input data were relatively similar. For example, the resulting explained variance and $RMSE_{xval}$ of all daily reconstructions remained below an absolute percent difference (APD) of 11% relative to one another, similarly reflected when comparing the week-composite reconstructions.

Table 2. Variance of $chla_{sat}$ dataset captured during DINEOF processing, including number of EOFs calculated and corresponding $RMSE_{xval}$ obtained. $RMSE_{xval}$ is also expressed in mg m^{-3}.

	Explained Variance (%)	**Calculated EOFs (#)**	**$RMSE_{xval}$ (log_{10} mg m^{-3})**	**$RMSE_{xval}$ (mg m^{-3})**
$D1_{2014}$	96.05	11	0.22	1.65
$D1_{2015}$	96.33	9	0.21	1.61
$D1_{2016}$	95.08	9	0.20	1.58
D3	97.08	26	0.17	1.49
$W1_{2014}$	68.99	3	0.32	2.07
$W1_{2015}$	74.68	3	0.30	1.98
$W1_{2016}$	73.52	3	0.29	1.95
W3	76.88	8	0.27	1.87

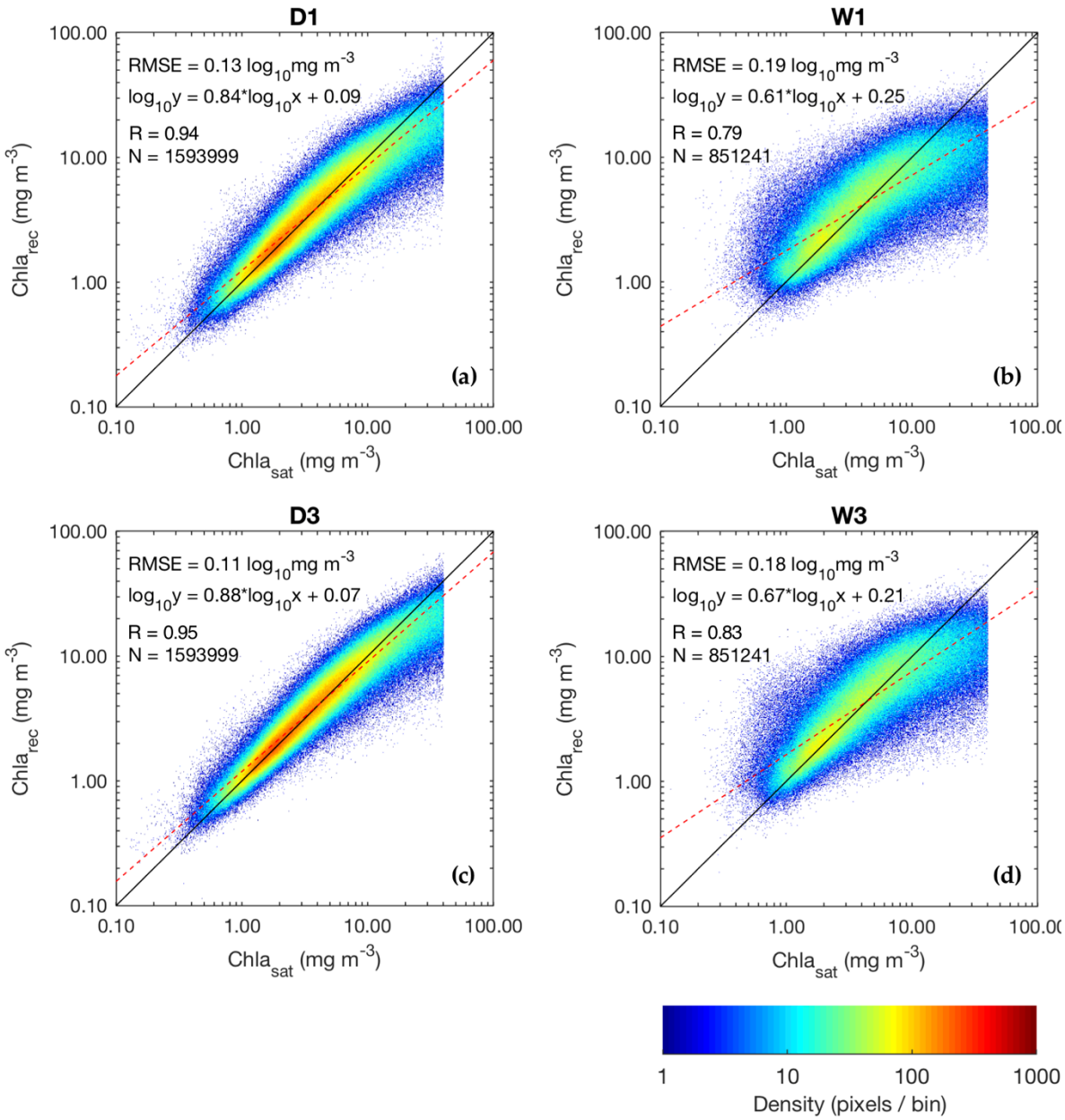

Figure 3. Linear correlation of all $chla_{sat}$ (x) with corresponding $chla_{rec\text{-}o}$ (y) pixels, encompassing all input data and cross-validation pixels, for the period 2014-2016. One-to-one line shown in black, with linear regression as red dashed line. D1 (a) and D3 (c) show better results relative to W1 (b) and W3 (d). The 40.00 mg m^{-3} threshold (section 2.2.1) is evident as a cutoff feature in all plots.

Similar to the global reconstruction results shown in Table 2, daily reconstructions were improved relative to week-composite, and multi-year relative to annual in terms of R, RMSE, slope and intercept for $chla_{rec\text{-}o}$ when correlated with

corresponding $chla_{sat}$ pixels for each one-year and three-year period for all DINEOF implementations. Specifically, D3 achieved better statistics relative to D1 when examined across the three-year study period (using all D1 *chla* pixels together, Figure 3a, 3c) and on a year-to-year basis, as $D3_{2014}$, $D3_{2015}$, and $D3_{2016}$ (Table 3a). Similar results were observed for W3 when compared to W1 reconstructions (Table 3b and Figure 3b, 3d), emphasizing the higher accuracy achievable for all pixels when time series with more input scenes were reconstructed. Considering all reconstructed datasets and time resolutions, D3 presented the best results overall, producing the lowest $RMSE_{xval}$ (0.17 $\log_{10}$ mg m^{-3}), lowest RMSE relative to $chla_{sat}$ pixels (0.11 $\log_{10}$ mg m^{-3} for all time resolutions), intercept nearest zero (0.07), highest R (0.95) and slope closest to 1.00 (0.88).

Differences in reconstruction accuracy year-to-year depended on the annual differences in input data (e.g., $chla_{sat}$ pixel values, image quality differences, spatial and temporal data coverage). These results show year-to-year differences correspond to the data coverage of each year, which differ due to natural causes, but are contributed to annually by natural events (such as forest fires). For example, of the three considered years, 2016 demonstrated the highest R and slope closest to 1.0 for the D3 (R 0.96, slope 0.89), W1 (R 0.81, slope 0.63) and W3 (R 0.84, slope 0.69) reconstructions (Table 3), corresponding to the year with lowest percent missing data (71.65% and 37.82% for $D1_{2016}$ and $W1_{2016}$, respectively; Table 1).

Table 3. Relationship of $chla_{sat}$ values to corresponding $chla_{rec\text{-}o}$ pixels per time period for daily (a) and week-composite (b) image time series. Statistics were retrieved for each three-year time series divided annually (forming $D3_{2014,2015,2016}$ and $W3_{2014,2015,2016}$).

(a)	R	RMSE (log_{10} mg m^{-3})	RMSE (mg m^{-3})	Slope	Intercept
$D1_{2014}$	0.94	0.13	1.35	0.85	0.08
$D3_{2014}$	0.95	0.11	1.29	0.88	0.07
$D1_{2015}$	0.93	0.13	1.35	0.83	0.10
$D3_{2015}$	0.95	0.11	1.29	0.87	0.07
$D1_{2016}$	0.93	0.13	1.35	0.84	0.09
$D3_{2016}$	0.96	0.11	1.29	0.89	0.07
(b)	**R**	**RMSE (log_{10} mg m^{-3})**	**RMSE (mg m^{-3})**	**Slope**	**Intercept**
$W1_{2014}$	0.78	0.20	1.58	0.59	0.25
$W3_{2014}$	0.84	0.19	1.55	0.67	0.20
$W1_{2015}$	0.79	0.19	1.55	0.59	0.27
$W3_{2015}$	0.82	0.18	1.51	0.64	0.23
$W1_{2016}$	0.81	0.19	1.55	0.63	0.23
$W3_{2016}$	0.84	0.18	1.51	0.69	0.20

The sensitivity test conducted by repeating DINEOF reconstructions with differing cross-validation points and subsets of each dataset revealed more clearly the dependence of global accuracy on the length of the input dataset used (Figure 4). For all implementations, calculated in log space but expressed here in units of mg m^{-3}, the mean variation (standard deviation) of $RMSE_{xval}$ remained below ± 1.00 mg m^{-3} and decreased as the size of the dataset increased toward the total original scenes. Variation of mean $RMSE_{xval}$ for the daily datasets was shown to be negligible as the number of scenes approached the full dataset size, producing consistently lower mean $RMSE_{xval}$ as the cross-validation points used and scenes removed for each trial were altered.

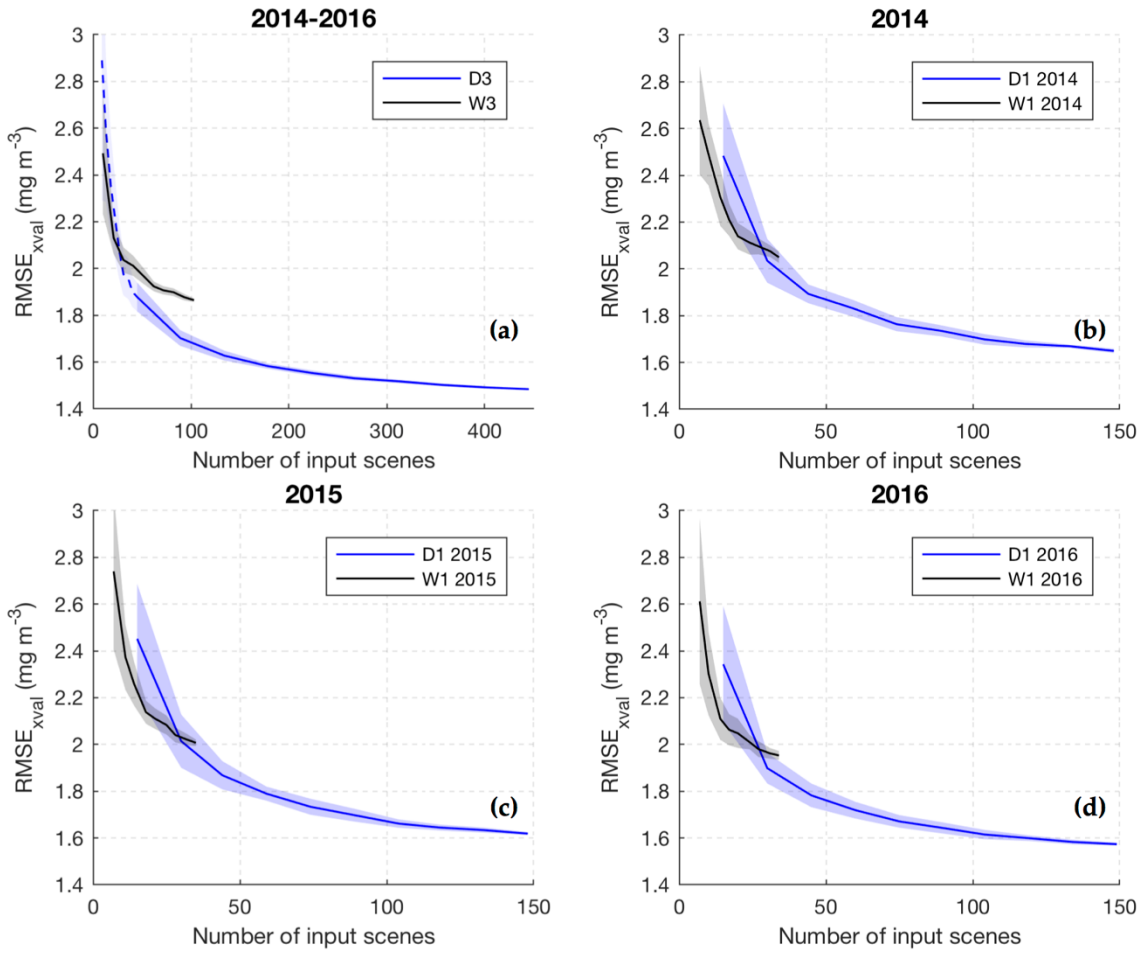

Figure 4. Mean $RMSE_{xval}$, with shaded ±1 standard deviation (mg m^{-3}), for daily (blue) and week-composite (black) results from repeated reconstructions, contrasting multi-year, D3 and W3 (a) and annual, D1 and W1 for 2014 (b), 2015 (c), and 2016 (d). As scenes were removed by proportion of datasets, minimum number of scenes are different for week-composite and daily; dashed line added for D3 to show results using fewer than 10% of the dataset. Note the change in scale of (a) x-axis.

Interestingly, the standard deviation of mean $RMSE_{xval}$ was lower for the week-composite than daily reconstructions when comparing identical numbers of scenes used as input to DINEOF, though in terms of realistic error of *chla* estimates, the magnitudes were negligible. For example, the standard deviation of D1 mean $RMSE_{xval}$ in 2014 was 0.06 mg m^{-3} for 34 scenes, while the corresponding W1 standard deviation was 0.02 mg m^{-3}. Additionally, the mean $RMSE_{xval}$ of week-composite reconstructions transitioned to

be lower than daily reconstructions at <30 input scenes. For example, when datasets of 25 randomly-selected scenes were processed with each DINEOF implementation used here, the retrieved mean $RMSE_{xval}$ was approximately 2.10 ± 0.06 mg m^{-3} for all week-composite reconstructions (Figure 4b), while the daily mean $RMSE_{xval}$ was 2.40 ± 0.20 mg m^{-3}. However, using so few scenes with DINEOF is generally not recommended (Alvera-Azcárate et al., 2005).

3.2. Spatio-temporal accuracy of DINEOF products

Spatially, the temporal R^2 values calculated between $chla_{sat}$ and $chla_{rec\text{-}o}$ for each three-year pixel time series were relatively consistent throughout the study region and higher for daily reconstructions, while lower and more variable for week-composite reconstructions (Figure 5). Specifically, the R^2 of the D1 reconstruction for all pixels was predominantly high (> 0.80), with the lowest values near the Fraser River discharge area (R^2 ~0.65 - 0.75, Figure 5a). This relationship was improved for D3 (R^2 predominantly > 0.90), with similar spatial pattern to D1, also reflecting the reduced relationship at the Fraser River plume area (R^2 ~0.70 - 0.85, Figure 5c). Conversely, week-composite $chla_{rec\text{-}o}$, which had much lower number of samples from which the statistics were calculated, showed much lower agreement to $chla_{sat}$ for each pixel time series, and did not demonstrate a spatially distinct area of lower values near the Fraser River, as observed with the daily input data (Figure 5b, 5d). The R^2 values remained below 0.80 for both W1 and W3, exhibiting high spatial variation and very low values in the PS region (R^2 < 0.4). The highest R^2 occurred in the JFS, QCS and northern SoG for W3 (~0.70, Figure 5d). W1, similarly, exhibited the highest relationship (R^2 ~0.60) in JFS and QCS. While per-pixel coverage was low for both the daily and week-composite

datasets for some regions of the Salish Sea (Figure 2c, 2d), very few R^2 pixels had p-values > 0.05, warranting removal from this analysis. Specifically, < 0.20% of the total Salish Sea pixels for week-composite data alone were removed.

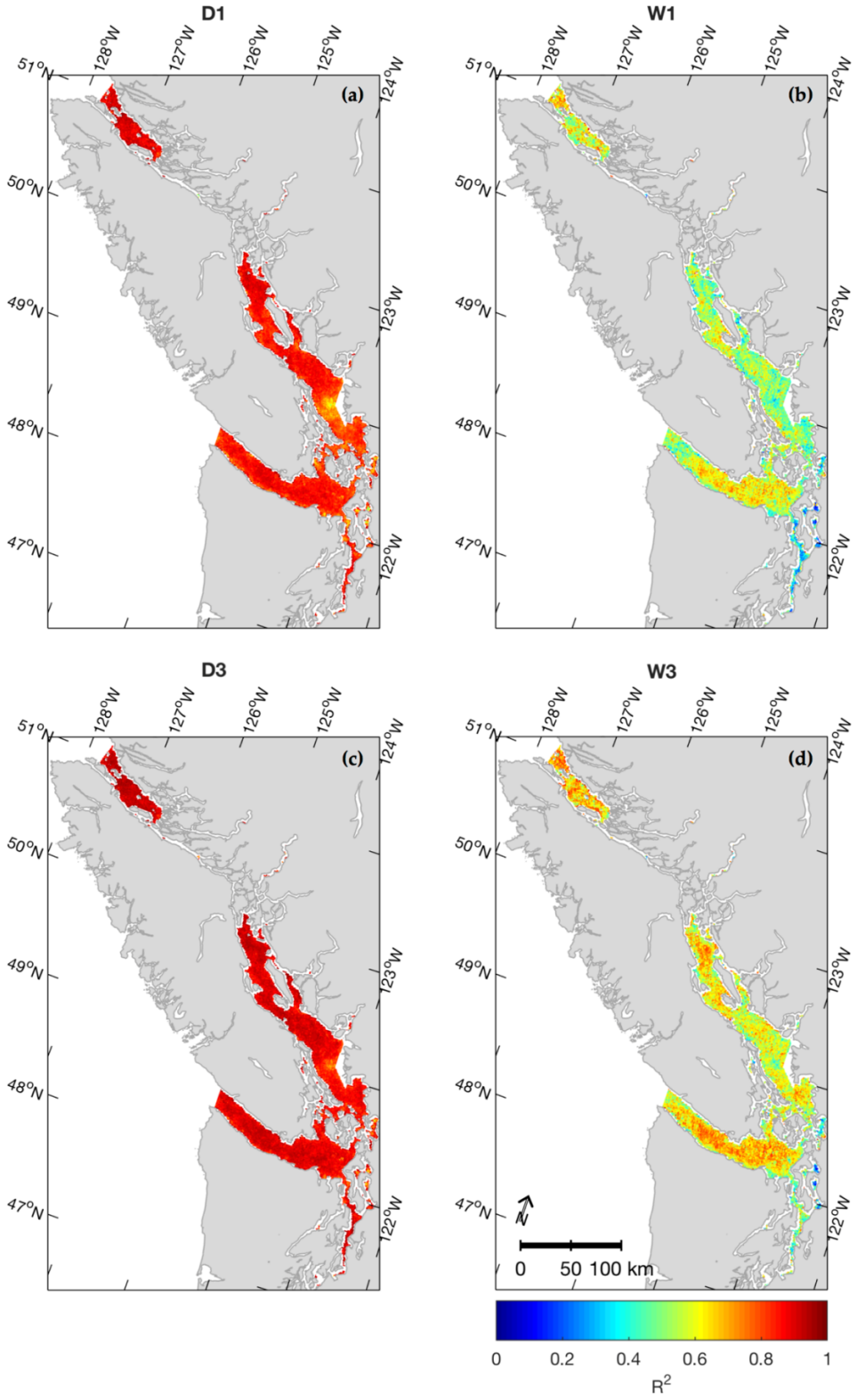

Figure 5. Per-pixel R^2 of DINEOF results for the full three-year study period: D1 (a), W1 (b), D3 (c) and W3 (d). Daily and week-composite pixel availability differed, impacting these results (Figure 2).

Temporally, differing reconstruction outcomes were evident in regions where no $chla_{sat}$ data were available previously. For example, a daily reconstruction from February 28th, 2014 is shown in Figure 6. The $chla_{sat+rec}$ pattern in the SoG differed between reconstructions, with D3 (Figure 6c) demonstrating a patch of low $chla_{sat+rec}$ at ~300 km along the thalweg not present in the D1 $chla_{sat+rec}$ image (Figure 6b). An example of a week-composite reconstructed image for the week of April 2nd, 2014 (Figure 7) similarly demonstrated *chla* of higher magnitude for W3 (Figure 7c), where $chla_{sat+rec}$ is > 25.0 mg m^{-3} at the entrance to the JFS, while W1 remained between 5.0 and 20.0 mg m^{-3} (Figure 7b). In this image W3 also reconstructed values below 1.0 mg m^{-3} in the SoG, while W1 is more consistent at approximately 2.5 – 5.0 mg m^{-3}. Figure 7a additionally demonstrates spatial heterogeneity of $chla_{sat}$ present in many week-composite scenes, resulting from the multiple daily scenes used for their construction.

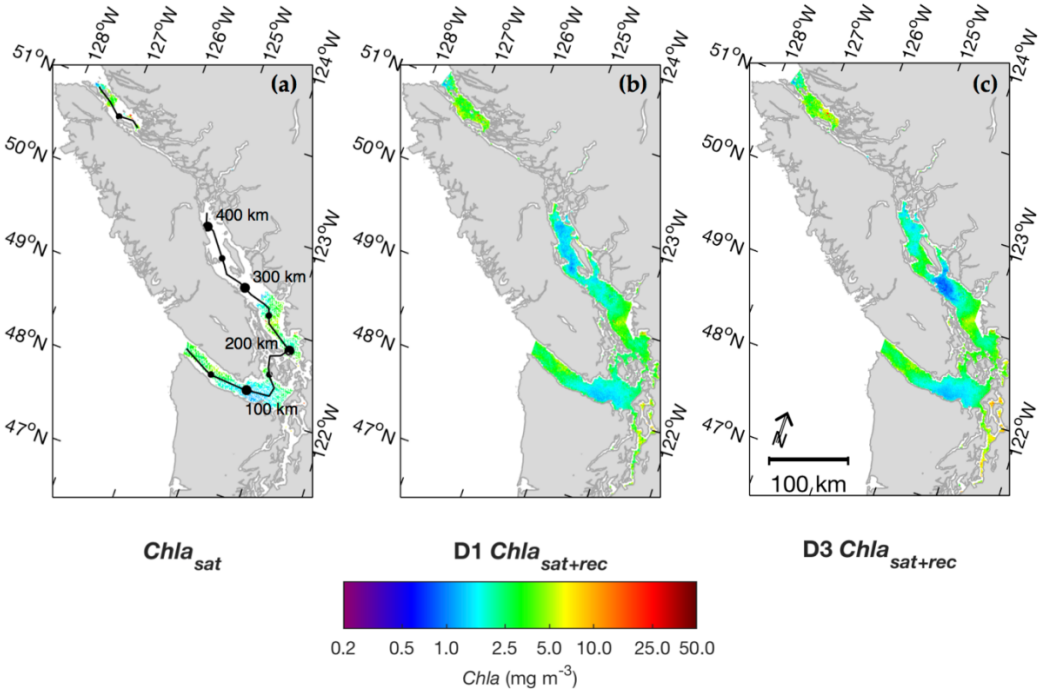

Figure 6. Example of daily reconstructions shown as the original $chla_{sat}$ (a), D1 $chla_{sat+rec}$ (b) and D3 $chla_{sat+rec}$ (c) of February 28th, 2014. Salish Sea thalweg is shown in (a), with a gap excluding Johnstone Strait due to the narrow passages in which satellite data was unresolvable.

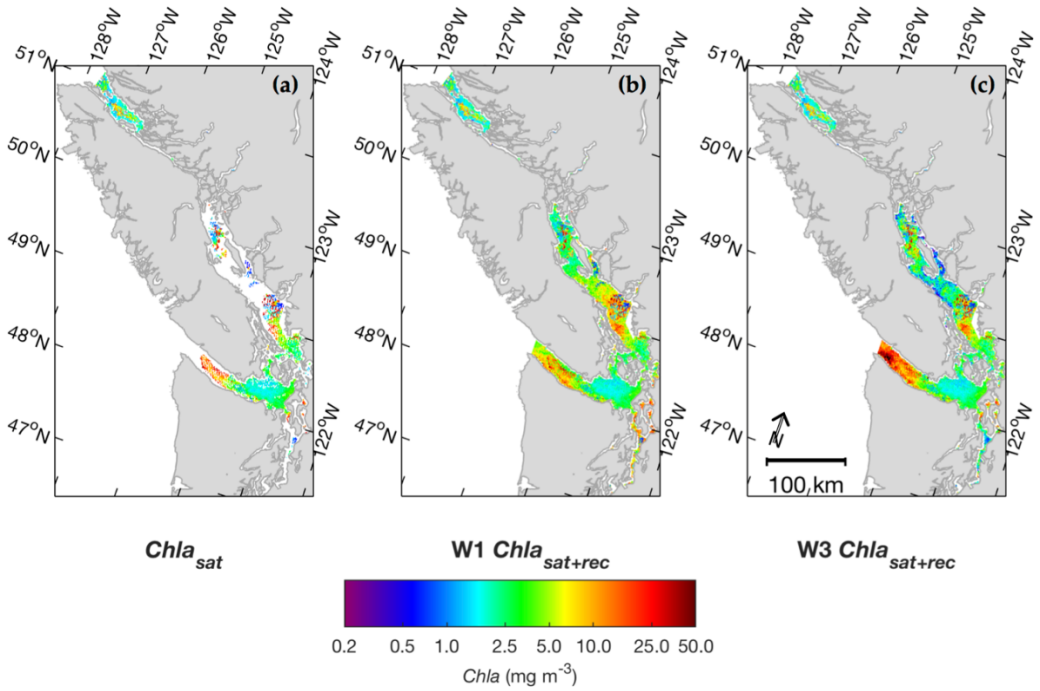

Figure 7. Week-composite reconstruction from the week of April 2nd, 2014: original $chla_{sat}$ (a), D1 $chla_{sat+rec}$ (b) and D3 $chla_{sat+rec}$ (c).

For another example, $chla_{sat+rec}$ along the Salish Sea thalweg for each time series are shown in Figure 8 and Figure 9. During spring of 2015 (late February through May), little spatial $chla_{sat}$ data was available for both daily and week-composite data in the Salish Sea north of ~250 km (Figures 8a, 9a, respectively). D1 reconstructed an event of high $chla_{sat+rec}$ lasting approximately 2 weeks during this period (Figure 8b), while the corresponding D3 time series demonstrated shorter duration and more localized high and low *chla* events (Figure 8c). For this time period, the week-composite $chla_{sat+rec}$ time series showed more similar results relative to one another (Figure 9 and additionally shown in Figure 13, Appendix B) due to the constrained temporal dimension and lower missing data present for each scene, though W1 demonstrated higher and lower magnitude *chla* events during this time (Figure 9b). These differences demonstrate that, while high accuracy of $chla_{rec\text{-}o}$ relative to original $chla_{sat}$ is achievable with DINEOF, the structures constructed where no spatial data existed previously are products of EOF calculations based on the input data alone, and can in turn impact further derived metrics such as bloom phenology.

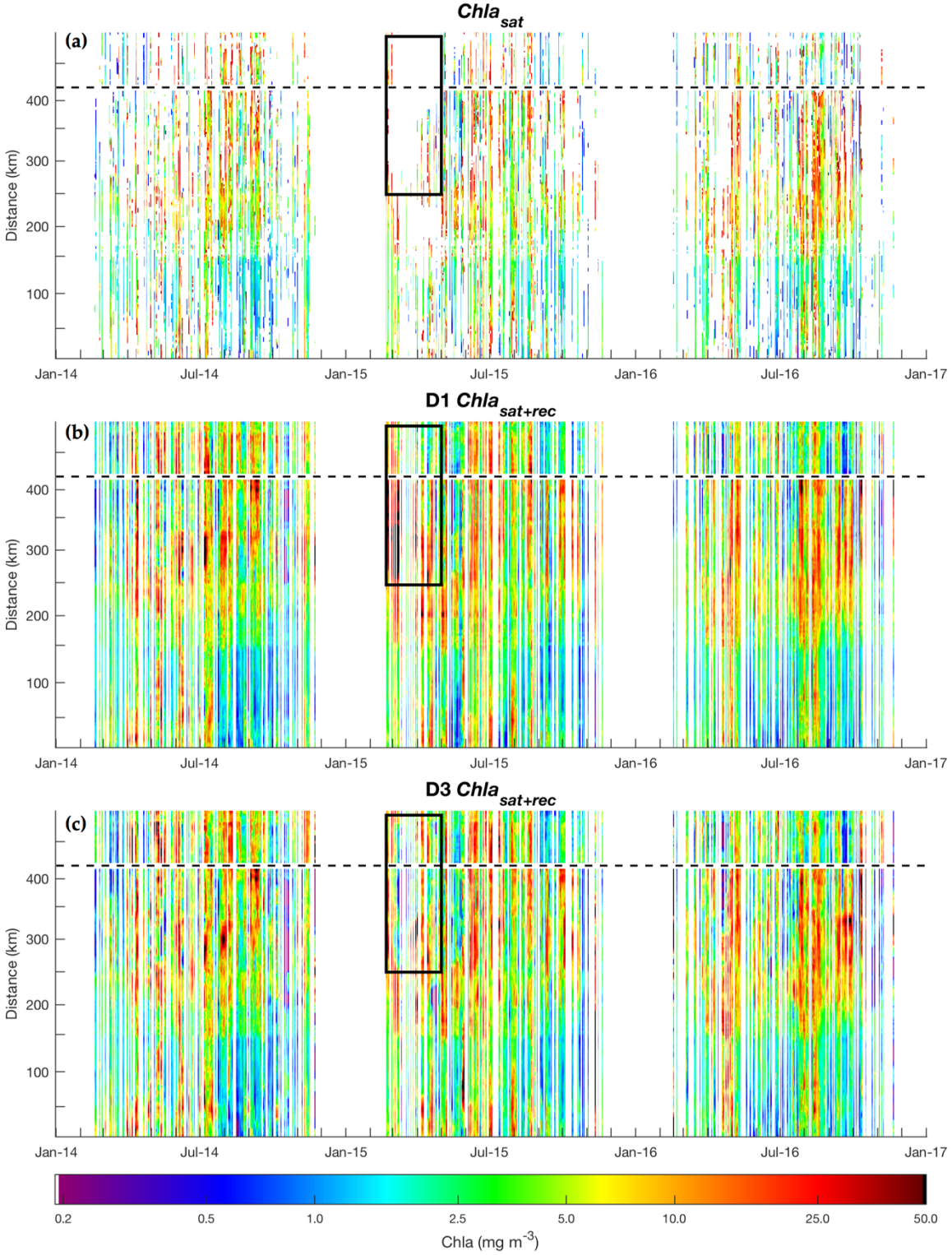

Figure 8. Daily time series shown as Hovmöller plot along Salish Sea thalweg, contrasting the original $chla_{sat}$ (a), D1 $chla_{sat+rec}$ (b) and D3 $chla_{sat+rec}$ (c) for 2014 – 2016. Dashed line represents spatial gap in Johnstone Strait due to inability of MODISA to resolve data in the narrow passages, and black square demonstrates time period of interest.

Y-axis represents distance along thalweg line, beginning in the south Salish Sea as seen in Figure 6a.

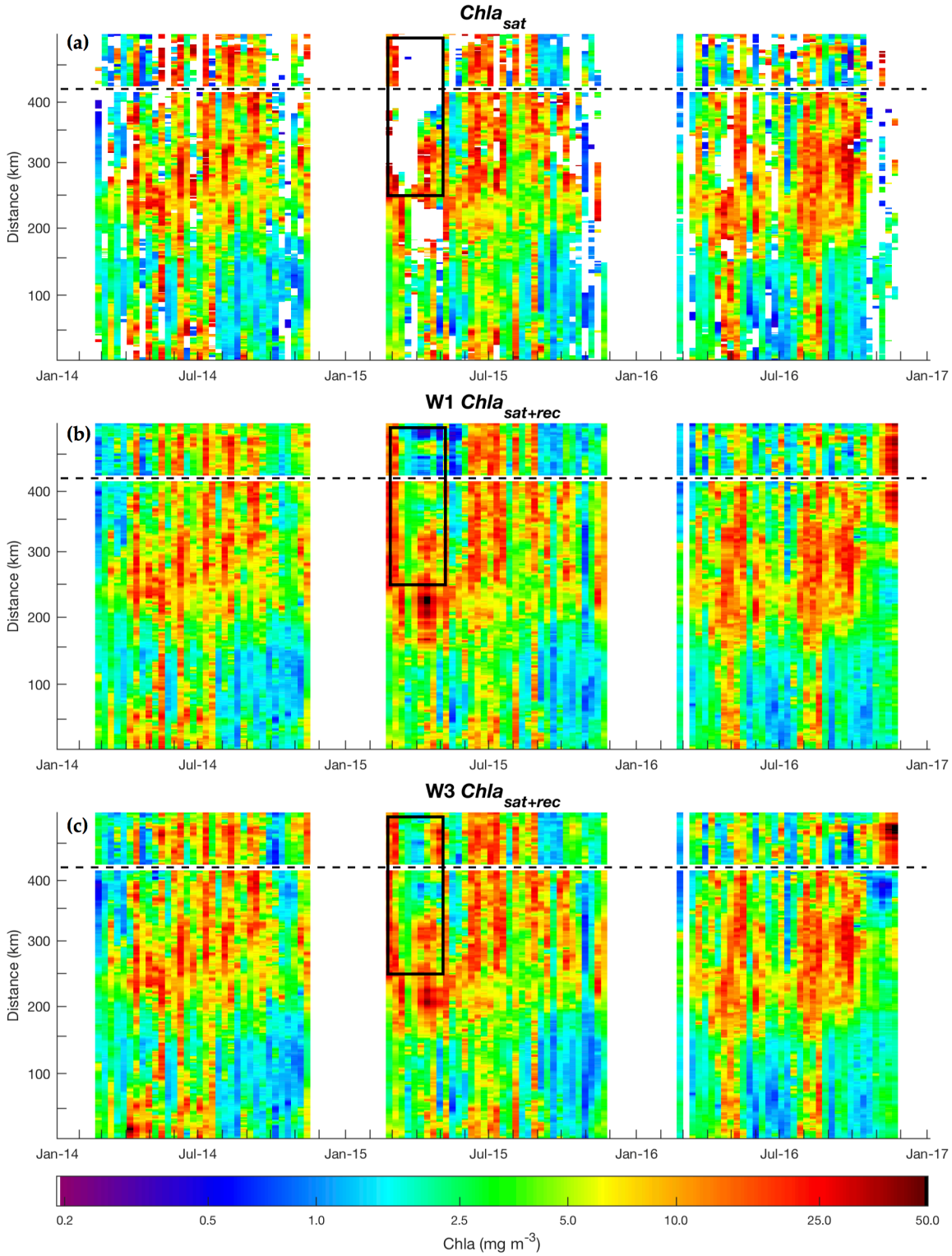

Figure 9. Week-composite time series extracted along the Salish Sea thalweg for $chla_{sat}$ (a), W1 $chla_{sat+rec}$ (b) and W3 $chla_{sat+rec}$ (c) for 2014 - 2016. Y-axis represents distance along thalweg line, beginning in the south Salish Sea as seen in Figure 6a. Black square representing time period of interest.

3.3. DINEOF-reconstructed and *in situ* data

From a total of 374 $chla_{insitu}$ samples acquired within ± 3 hours of daily satellite scenes, 15 and 45 were available for the validation of the original satellite-derived $chla_{sat}$ and the DINEOF output $chla_{sat+rec}$ datasets, respectively. $chla_{insitu}$ matchup values corresponding to $chla_{sat}$ matchups ranged from 1.19 - 12.17 mg m^{-3} (median 2.26 mg m^{-3}), and the $chla_{insitu}$ matchups correlated with the reconstructed $chla_{sat+rec}$ ranged from 0.54 – 26.90 mg m^{-3} (median 2.55 mg m^{-3}). The satellite- and DINEOF-derived concentrations corresponding to these $chla_{insitu}$ ranged from 1.30 – 18.00 mg m^{-3} for $chla_{sat}$ (median 5.40 mg m^{-3}), 0.98 – 77.34 mg m^{-3} for D1 $chla_{sat+rec}$ (median 5.16 mg m^{-3}), and 0.68 – 23.43 mg m^{-3} for D3 $chla_{sat+rec}$ (median 5.44 mg m^{-3}). Note that while $chla_{sat}$ pixels greater than 40 mg m^{-3} were removed (section 2.2.1), reconstructed pixel values were not filtered in this manner for the analysis, allowing higher concentrations to be present. However, these corresponded to <1% of the total pixels, though ended up reflected in one of the D1 matchups.

The statistical results showed that, in general, both $chla_{sat}$ and $chla_{sat+rec}$ values were overestimated relative to the $chla_{\text{insitu}}$ (Figure 10). $chla_{sat}$ achieved the highest R (0.69), slope nearest 1.0 (0.61), and lowest RMSE (0.23 $\log_{10}$ mg m^{-3}) relative to the $chla_{insitu}$. For the $chla_{sat+rec}$, the D1 matchups produced a higher R (0.48) and slope closer to 1.00 (0.55) than the D3 $chla_{sat+rec}$, and achieved the poorest RMSE (0.39 $\log_{10}$ mg m^{-3}). P-values calculated for all correlations remained below 0.05, signifying statistical significance of the relationships.

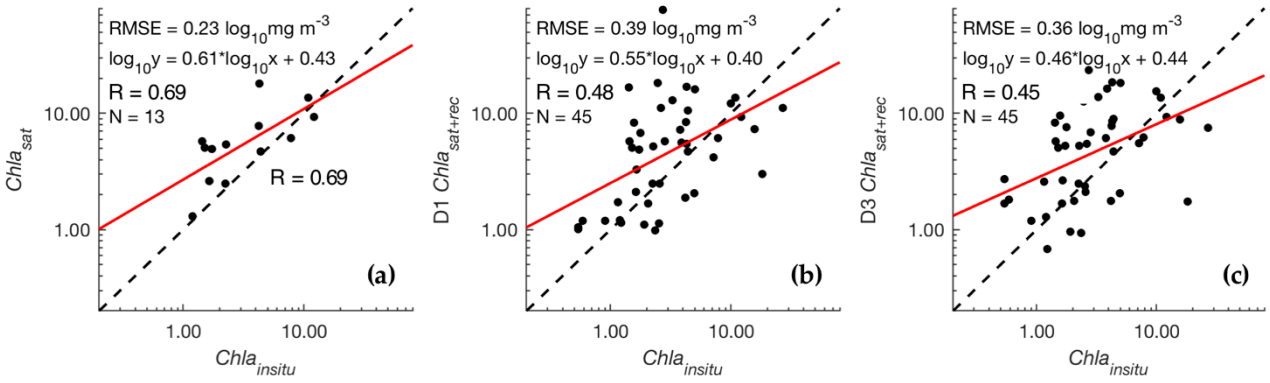

Figure 10. *chla*$_{insitu}$ matchups contrasted between *chla*$_{sat}$ (a), D1 *chla*$_{sat+rec}$ (b) and D3 *chla*$_{sat+rec}$ (c) reconstructions.

4. Discussion

The following sections provide a discussion of these results and considerations for using the DINEOF method, particularly for datasets of shorter time span. The accuracy and relationship of all satellite products to the available *in situ* samples is discussed relative to previous regional results and similar studies in other regions of the world.

4.1. Satellite-derived vs. DINEOF-reconstructed *chla*

This research presents the analysis of DINEOF reconstructions of MODISA *chla* products for an optically dynamic coastal water body on the west coast of Canada. In this study, the temporal dimension and spatial coverage of input data used with the DINEOF method were addressed. Overall, the daily input time series (D1 and D3) produced more accurate *chla* reconstructions relative to week-composite time series. Additionally, longer time periods (three-years rather than 1-year input data) produced improved reconstructions. When repeating all reconstructions and simulating datasets of lower temporal coverage for each time period and data form, the global accuracy remained relatively consistent, demonstrating the general effectiveness of the iterative and convergence-based processing of the DINEOF method. Compared to *in situ* matchups, as

expected, original $chla_{sat}$ achieved a better relationship than the reconstructed $chla_{sat+rec}$, though far fewer matchup data were available for the former.

While there are many factors that impact the outcomes when using this method for spatial reconstruction of satellite datasets, including the study area extent and processing parameters used, our results can be explained mainly by the following:

1. A higher number of valid $chla_{sat}$ pixels allow physical processes to be more clearly resolved in time and space. As the degrees of freedom increase with longer time series, a higher number of EOFs can be calculated (Alvera-Azcárate et al., 2009; Taylor et al., 2013). Consequently, finer-scale features (e.g., spatially localized events of shorter duration) and greater variance of the input dataset are captured, thus improving the accuracy of the reconstruction.
2. Processes that are poorly represented are more difficult to reconstruct. Week-composite scenes often displayed spatially discontinuous features reflecting the varied spatial and temporal daily $chla_{sat}$ scenes used in the binning process, similarly discussed in other studies (Sirjacobs et al., 2011). EOF reconstruction methods usually produce spatially smoothed datasets, making spatial discontinuities such as the ones observed on week-composites more difficult to capture, particularly when only few EOF modes are calculated due to dataset size constraints.

As a result, longer time series (e.g., D3 over D1, and W3 over W1) produced the best DINEOF outcomes, with D3, the input time series with most overall valid pixels and images, producing the best results (Tables 2, 3). The shortest time series (W1), on the other hand, likely did not contain sufficient images (Table 1) to capture enough information to reflect physical processes in so few EOFs (Alvera-Azcárate et al., 2009).

For example, while 26 EOFs were calculated for D3, combining to capture 97.08% of the variance of the original input dataset, only three EOFs were calculated for each W1 year, capturing from 68.99% - 74.68% of the input dataset variance.

The improved DINEOF results of daily input data were also evident when examining the temporal relationship between $chla_{sat}$ and $chla_{rec\text{-}o}$ throughout the study region (Figure 5). For D3 and D1, Figures 5a and 5c show an $R^2 > 0.80$ for most of the Salish Sea, however, a spatial region of lower reconstruction effectiveness where R^2 ~0.75 for D3 and ~0.60 for D1 occurred nearest the Fraser River plume. Here, *chla* is consistently high as shown by *in situ* data (Halverson & Pawlowicz, 2013; Loos & Costa, 2010; Phillips & Costa, 2017) and satellite-derived *chla* (Carswell et al., 2017; Jackson et al., 2015). Fraser plume waters are also documented to negatively impact retrievals of OC3M *chla* (Komick et al., 2009), which may have reduced the range of *chla* in the temporal domain, with consequences to the daily DINEOF reconstructions. DINEOF reconstructions have been demonstrated to perform better in regions of high temporal variability or gradients, as opposed to more homogeneous waters, with results of previous studies reasoning that a more dramatic signal can be observed, and thus, more effectively reproduced for such regions (Sirjacobs et al., 2011; Wang & Liu, 2014). In our case, lower R^2 may have been a result of less variable $chla_{sat}$ over the time series nearest the Fraser River plume relative to other regions of the Salish Sea.

The greater homogeneity of *chla* in this region is evident in Figures 8 (a, b, c) and 9 (a, b, c) as *chla* consistently greater than ~5.00 mg m^{-3} (located at ~ 250 km distance along the Salish Sea thalweg), and through a closer look at the relationship between D3 $chla_{sat}$ and $chla_{rec\text{-}o}$, with emphasis on the Fraser plume waters (Figure 11). *chla*

concentrations are more homogeneous, ranging between ~3.00 and 13.00 mg m^{-3}, compared with, for example, the JFS, where concentrations ranged from 0.40 - 40.00 mg m^{-3} and an improved linear relationship was observed (R 0.95 over 0.88, RMSE of 0.09 $\log_{10}$ mg m^{-3} over 0.10 $\log_{10}$ mg m^{-3}, slope of 0.86 over 0.74). The corresponding W3 $chla_{sat}$ and $chla_{rec\text{-}o}$ data for the same regions are shown, with poorer relationship (e.g., R 0.60 for Fraser River plume and 0.89 for JdF) compared to D3, though representing a similar range of concentrations as observed with the D3 reconstruction (Figure 11c, 11d).

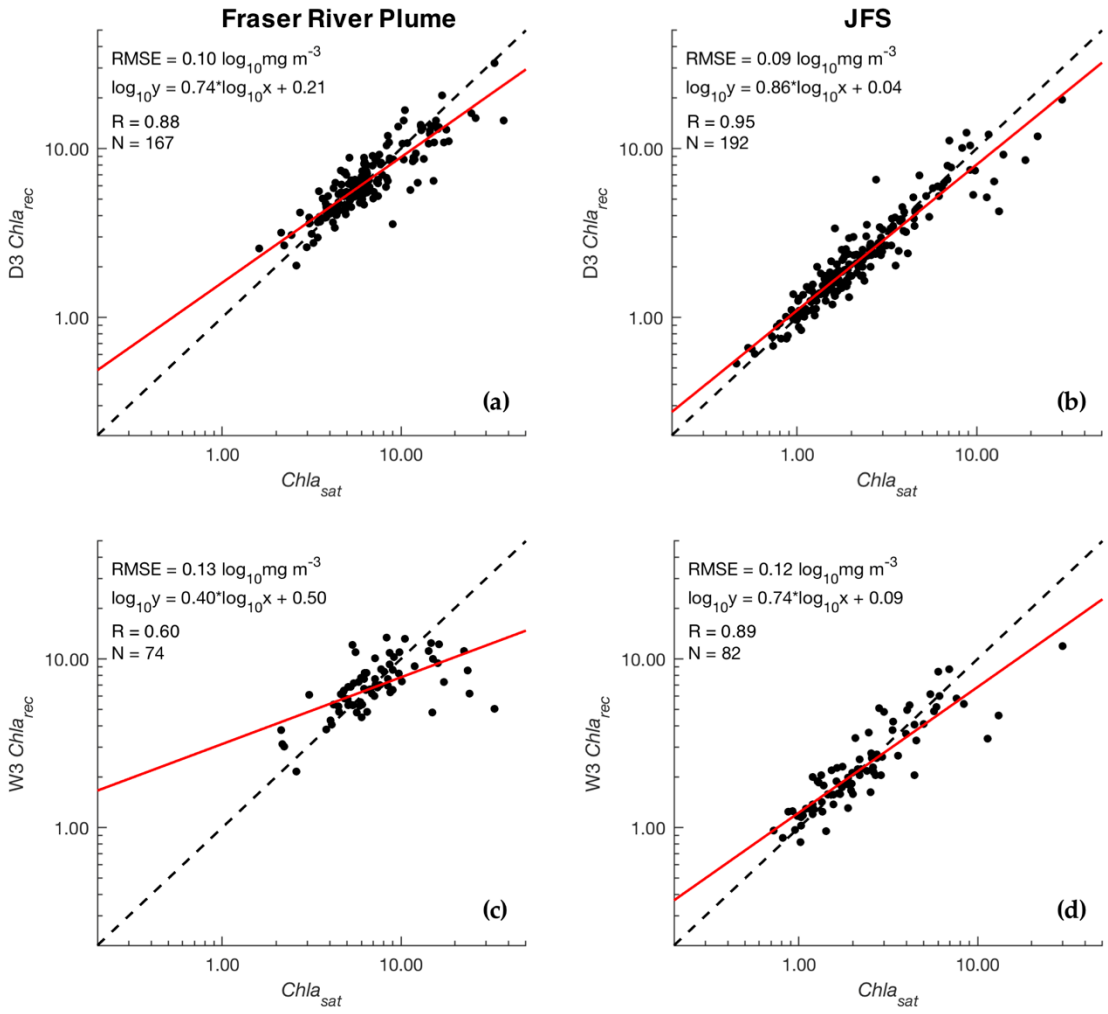

Figure 11. Example relationship between original ($chla_{sat}$) and reconstructed ($chla_{rec\text{-}o}$) pixel time series for a D3 pixel in the Fraser River plume (a) and in central JdF (b). These are contrasted with the same locations from the W3 reconstruction as (c) and (d), respectively.

The poorer performance of week-composite reconstructions may be contrary to expected considering the much higher spatial coverage per image when compared to daily images. As shown here the greatly reduced temporal dimension (Table 1), combined with higher spatial heterogeneity of *chla* (Figures 5b, 5d, 7a) resulted in poorer reconstructions. Therefore, week-composite data for input are inferior to use with DINEOF when daily data are available for the same time period (for three-years or less).

However, in studies for longer time series, week-composite data may be preferable where the temporal and spatial scale of features wishing to be resolved are not negatively impacted by the lower temporal coverage. As shown in Figure 13 (Appendix B), the spatio-temporal time series of W1 and W3 were very consistent relative to each other, as compared to the daily $chla_{sat+rec}$ time series, which demonstrated greater differences in image median and standard deviation values between, $chla_{sat,}$ D1 and D3. This is in part due to the higher spatial coverage of $chla_{sat}$ present in the week-composite scenes, which reduces impact of reconstructed values on these image statistics. Further research should include comparison of reconstructed week-composite images relative to week-composites made from reconstructed daily images as used in some studies (e.g., (Marchese et al., 2017)).

Among the daily reconstruction results, annual reconstructions (D1) and three-year reconstructions (D3) produced very comparable correlations between $chla_{sat}$ and $chla_{rec\text{-}o}$ (Table 3a, Figure 3a, 3b), similar $RMSE_{xval}$ of reconstruction and throughout the sensitivity test (Table 2, Figure 4), and high per-pixel temporal R^2 (Figure 5). D1 results, however, demonstrated several improved outcomes for further consideration. D1 demonstrated a slightly better R relative to D3 $chla_{insitu}$ matchups (0.48 over 0.46) in addition to slope closer to 1.00 (0.55 over 0.46) and lower intercept (0.40 $\log_{10}$ mg m^{-3} over 0.44 $\log_{10}$ mg m^{-3}). The number of optimal EOFs calculated for each D1 year (see section 2.3.2) was lower (2014: 11, 2015: 9, 2016: 9) than those calculated for the D3 reconstruction (26), yet nearly equivalent variance of the $chla_{sat}$ datasets was captured (Table 2) in faster processing time (D1 processing was ~4 times faster for all 3 years). While many more EOFs were calculated for D3, the final 5 contained less than 4% of the

dataset variance (Appendix A). Additionally, calculating more EOFs is not always better, as separability of the EOF modes declines as more are calculated, and there is a higher likelihood of representing patterns found in the dataset that may not exist in reality (Strang, 1988). This was a particular consideration for this dataset, as anomalous phytoplankton blooms occurred in the Salish Sea during the study period. Further, limiting the distribution of input $chla_{sat}$ concentrations by year eliminated long winter gaps, which led to better constrained EOFs. Note an example of this in Figure 13 (Appendix B), which demonstrates the effect of long winter gaps in this time series on the per-scene median and standard deviation. D3 exhibited erroneously high $chla_{sat+rec}$ median and standard deviation in some images (e.g., 16.00 ± 12.00 mg m^{-3} in November, 2015) compared with D1 (3.00 ± 3.50 mg m^{-3} at corresponding time), though in some cases the original $chla_{sat}$ is also high, where the D1 reconstruction serves to lower the median and standard deviation. Given the advantages explained above, the annual input data is a preferable alternative to multi-year input data when using datasets with long winter gaps and dynamic spatiotemporal phytoplankton phenology.

The impact of time period input to DINEOF was additionally examined by performing a sensitivity test to simulate datasets of fewer input scenes over annual and multi-year time periods. Similar to the findings reported in (Ganzedo et al., 2011), the output $RMSE_{xval}$ calculated was dependent on the distinct dataset lengths (Figure 4, Table 2). For input datasets of sufficient number of input scenes (here >100 images), the $RMSE_{xval}$ remained low and stable, showing a low standard deviation (Figure 4) that increases with smaller dataset sizes. However, depending on the desired global accuracy of a study, even using few input scenes relative to the time period (e.g., 50 scenes over

three years), a relatively low $RMSE_{xval}$ is achievable (Figure 4a). Within the achieved $RMSE_{xval}$, the daily input dataset produced lower values than the week-composite. However, at very small dataset sizes (< ~30 images), the test demonstrated a transition where $RMSE_{xval}$ was lower for week-composite reconstructions (Figure 4). This is due to multiple factors: daily time series have higher probability of lengthy gaps between image dates, thus reducing the spatial coherence between images used for the reconstruction; and, the percent of missing data was generally more uniform for the week-composite time series, and consequently, more EOFs than daily input data were calculated in some cases at these small input dataset sizes. (Ganzedo et al., 2011) found similar number of input scenes (35) to achieve the minimum needed for stable RMSE when reconstructing SST data. However, using DINEOF with so few input data are generally not recommended due to the low number of degrees of freedom and the decreased ability to capture physical trends (A. Alvera-Azcárate et al., 2005). This makes the adoption of annual week-composite $chla_{sat}$ not recommended for DINEOF reconstruction due to the low number of input scenes. Nonetheless, as demonstrated in our results (Figures 3, Table 2 and Table 3) the statistics and time series produced with W1 reconstructions were comparable to the three-year (Table 2, 3).

While this study provides insights on the effects of the data form and length of the input time series on DINEOF outcomes, other factors that impact reconstruction outcome accuracy include the length of temporal data gaps (i.e. consecutive missing days or weeks), quality controls of input data (e.g., detection and removal of outliers, minimum coverage per scene requirement), study area extent, and parameters used to reconstruct the dataset (e.g., temporal covariance filter length). For example, the cross-validation

method used to define the EOFs in this study produced consistent global accuracy, which was evidenced with repeated DINEOF tests (Figure 4). While cloud-shaped cross-validation clusters have been used in some DINEOF applications (Beckers et al., 2006; Nechad et al., 2011), this method was found to be less effective for this dataset (fewer modes calculated, lower explained variance; results not shown). Additionally, when considering the temporal pattern of input scenes, the order of images should not impact the reconstruction results (A. Alvera-Azcárate et al., 2005; Mauri, Poulain, & Notarstefano, 2008); however, as illustrated with our dataset, long gaps between scenes, such as periods of missing data during winter months, can lead to calculation of irrelevant EOFs and unrealistically high/low *chla* and temporal discontinuities in *chla* concentration from image-to-image (Figure 13, Appendix A), similar to results by (Alvera-Azcárate et al., 2009). Without further adjusting the quality controls used in this study (e.g., stricter image processing flags, higher minimum percent of image pixels required) this may be avoided by using a longer time series (more years) to better constrain the EOFs near long gaps, or with the use of a longer temporal covariance matrix filter to better remove spurious signals of short duration from the temporal EOFs (Alvera-Azcárate et al., 2009).

The quality of input data is perhaps one of the most important considerations for the accuracy of DINEOF outputs. For this study, $chla_{sat}$ is used as 'reference' to which DINEOF-calculated pixels are compared, yet any satellite product already possesses uncertainties (Land et al., 2018). In this study, quality control prior to DINEOF processing included standard ocean-colour flags, in addition to a reduced straylight filter (3x3) (which significantly increased the number of usable $chla_{sat}$ pixels), removal of $chla_{sat}$ pixels exceeding 40.00 mg m^{-3} (section 2.2.1), and removal of scenes and pixels

with less than 2% ocean coverage (section 2.3). However, outlier or erroneous pixels, particularly at undetected cloud-edges or contrails (Meister et al., 2008), may have been introduced through the straylight flag alteration, or in low quality scenes / scenes with low spatial coverage. A relationship between the number of pixels in an original *chla* image and the reconstructed pixel effectiveness was observed (Figure 12), suggesting that reconstructions are poorer for scenes with lower spatial coverage, as they are more likely to be composed of low-quality pixels and statistically contain fewer pixels used for cross-validation. By raising the minimum coverage (for example, at least 5% spatial coverage, which is used in many DINEOF implementations) improved reconstruction may be achieved by removing the impact of these scenes on the calculation of EOFs, though in this study a significant number of scenes were already removed with the 2% minimum coverage used (Table 1). Additionally, the removal of pixels exceeding 40.00 mg m^{-3}, while consistent with other remote sensing *chla* studies of the region (Carswell et al., 2017; Jackson et al., 2015), resulted in a distinctive cutoff of the distribution of input data (Figure 3). This led to a reduction of the global input dataset mean, and as a result, DINEOF-calculated pixels demonstrated a tendency to under-estimate $chla_{rec\text{-}o}$ concentrations above ~10 mg m^{-3} as data are reconstructed following a normal distribution of the input dataset anomaly (section 2.3.1). Beyond the quality control methods for input data used here, other techniques include limiting the number of scenes per month for temporal consistency (Mauri et al., 2007), down-sampling data resolution to reduce outliers (Mauri et al., 2008, 2007), more strict spatial coverage requirements (e.g., 10% spatial coverage (Mauri et al., 2008)), and various methods for statistical detection and removal of outlier pixels (Alvera-Azcárate, Sirjacobs, Barth, & Beckers,

2012; Alvera-Azcárate et al., 2015; Sirjacobs et al., 2011; Wang & Liu, 2014). These methods, the latter in particular, are recommended for further use. For example, the impact of spatial heterogeneity observed in the $chla_{sat}$ week-composite scenes of this study (Figure 7a), introduced from averaging multiple daily images, can be reduced (e.g., reducing the spread of pixels evident in Figure 3b, 3d) if statistical outlier pixels are mitigated in a more robust manner.

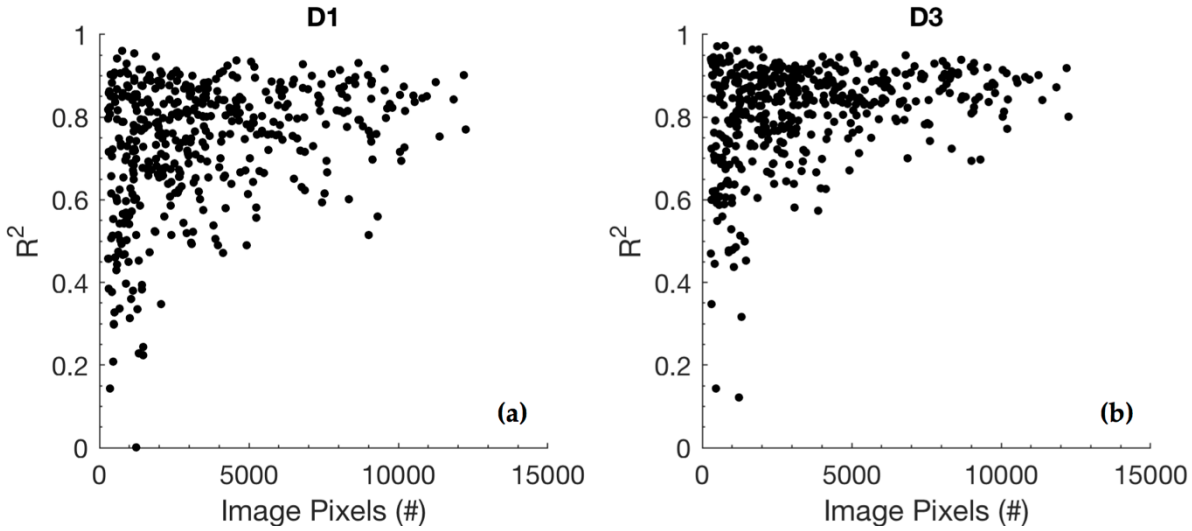

Figure 12. R^2 (y-axis) vs. number of $chla_{sat}$ pixels (x-axis) per image for daily reconstructions. Both (a) D1 and (b) D3 for 2014 - 2016 have a higher probability of low R^2 in scenes with fewer pixels in the original image.

In addition to stricter quality-control of input data for improving data reconstructions, higher accuracy with DINEOF can be achieved by exploiting correlations with other oceanographic variables. For example, multivariate DINEOF applications to *chla* paired with SST have produced more accurate SST results when compared to univariate DINEOF (Alvera-Azcárate et al., 2007; Miles et al., 2009), and may reduce the impact of study period on the reconstruction accuracy (Alvera-Azcárate et al., 2007). Other implementations of DINEOF have utilized a moving temporal

window (Corredor-Acosta et al., 2015), rather than reconstructing distinct time periods as shown in this study, and modifications to DINEOF have also been implemented with improved results, such as the DINEOF-OI setup of (Beckers, Barth, Tomazic, & Alvera-Azcárate, 2014).

4.2. Accuracy of $chla_{sat}$ and reconstructed products

The accuracy of the satellite- and DINEOF-derived products used in this study were assessed relative to available *in situ* matchups for the region during this time period, to other ocean-colour studies, and relative to results of similar DINEOF studies. Units here are expressed as mg m^{-3} to be comparable across studies. The original $chla_{sat}$ matchups produced RMSE of 1.70 mg m^{-3} (R 0.69) and DINEOF-reconstructed $chla_{sat+rec}$ produced RMSE of 2.45 mg m^{-3} (R 0.48) and 2.29 mg m^{-3} (R 0.45) for D1 and D3, respectively (Figure 10). The $chla_{sat}$ results are within the global OC3M RMSE for MODISA *chla* (2.10 mg m^{-3}) ("NASA Ocean Color," n.d.). Specifically, our RMSE results are comparable to previous studies in the Salish Sea, where MODISA-derived *chla* have shown RMSE values of 2.14 mg m^{-3} (R 0.73) compared with *in situ* extracted *chla* (Carswell et al., 2017) and 2.63 mg m^{-3} (R 0.85) compared with ferry-measured *in situ* fluorimetric measurements (Komick, 2007). While the reconstructed RMSE are higher, these values are of similar magnitude to (Wang et al., 2015), where a better RMSE for the original *chla* was achieved (1.80 mg m^{-3}) relative to DINEOF-reconstructed SeaWiFs *chla* (2.50 mg m^{-3}) for the Yangtze River estuary.

When examining the metrics for assessing accuracy of the reconstructions (e.g., $RMSE_{xval}$, RMSE of $chla_{rec\text{-}o}$ to $chla_{sat}$), the results are within published satellite-derived *chla* concentration measures, though the reconstructed *chla* shows both over- and under-

estimation across the range of concentrations (Figure 10). This is likely largely due to spatial biases of the available *in situ* data, combined with inherent inaccuracies of standard bio-optical algorithms for MODISA in complex coastal environments (Bailey & Werdell, 2006). The matchups used here were mostly from waters under the influence of the Fraser River plume, where OC3M *chla* estimates are negatively impacted (Carswell et al., 2017; Komick et al., 2009; Komick, 2007). High concentrations of suspended matter, in addition to tidal activity, wind and river discharge, make this region dynamic and optically complex (Loos & Costa, 2010), adding difficulties to accurate time/space matchups and satellite retrievals, and consequently, to the DINEOF reconstruction. For instance, scattering from high concentrations of TSM can result in loss of valid satellite pixels or erroneous estimation of *chla*, which leads to higher discrepancies when compared to *in situ* extracted *chla* (Carswell et al., 2017; Komick, 2007). An important reminder is the low number of *in situ* matchups, which is a limitation for validation of satellite data, including DINEOF-reconstructed datasets. Continuous or relatively stationary *in situ* time series datasets, such as buoy data, may be more appropriate for validating DINEOF and discerning its utility for replicating trends, as compared to spatially varied, discrete *in situ* extracted samples.

The retrieved $RMSE_{xval}$ statistical error during the DINEOF reconstructions and global RMSE from linear correlation give simple measures of global reconstruction accuracy. D3, which demonstrated the best reconstruction results, showed an $RMSE_{xval}$ of 1.49 mg m^{-3}. Roughly, each reconstructed value should be within this magnitude of the true *chla* values. Given the high percentage of missing data, and varied $RMSE_{xval}$ reported in other DINEOF *chla* studies using both daily and week-composite input data

(e.g., 0.60 mg m^{-3} (Mauri et al., 2007), 1.23 mg m^{-3} (Marchese et al., 2017), 1.55 mg m^{-3} (Sirjacobs et al., 2011), or lack thereof of accuracy mentioned (McGinty et al., 2016; Waite & Mueter, 2013)), the RMSE of all presented reconstructions is within acceptable ranges. The RMSE achieved from $chla_{sat}$ and $chla_{rec\text{-}o}$ linear correlations of week-composite data, while the lowest of the datasets reconstructed (1.87 – 2.07 mg m^{-3}), is comparable to the results of the *in situ* samples with OC3M *chla*, and is below the global OC3M RMSE of 2.10 mg m^{-3}.

Conclusions

Derivation of phytoplankton phenology from satellite sensors is challenged by missing data (Corredor-Acosta et al., 2015), as few places are free of cloud-cover or conditions that impede detection of light leaving the ocean surface (King, Platnick, Menzel, Ackerman, & Hubanks, 2013). In this study, a reconstruction technique for filling spatial gaps in geophysical datasets, Data Interpolating Empirical Orthogonal Functions (DINEOF), was applied to Salish Sea satellite-derived *chla* products spanning a three-year time period. This study investigated the effects of varying the dataset study period and forms of input data (daily vs. week-composite) used for DINEOF reconstructions, as the outcomes influence further uses of reconstructed datasets.

The current study demonstrated that the temporal dimension of a dataset is the major factor for the effectiveness of the *chla* reconstruction accuracy. Specifically, the greater spatial coverage of week-composite dataset is not an advantage for *chla* reconstruction relative to the corresponding daily image time series for a given study period. The daily time series will always contain more scenes and overall available data points, which facilitates the calculation of a higher number of EOFs, thus capturing

higher variance of the original dataset. The greater spatial heterogeneity of week-composite imagery combined with low number of scenes for this study period led to inferior results. Additionally, annual study period constraints for DINEOF processing were imposed. For daily input data, these implementations were faster to process, with the advantage of annually constraining the EOF basis (distribution of *chla*). Daily reconstructions resulted in clear advantages for the short time series used in this study (three years). However, for decade-scale studies, daily data may be unnecessary when week-composite data is available, as the greatly increased number of week-composite input scenes should produce reasonable accuracy. When utilizing matchup data as to validate the daily input $chla_{sat}$ and reconstructed $chla_{sat+rec}$ imagery, measures of error were comparable to other studies where *chla* was retrieved with the OC3M method for the study region, and with global datasets. In addition, while *chla* remains difficult to reconstruct and further quality control improvements are necessary for this dataset, the global accuracies of the $chla_{rec-o}$ contrasted to the original $chla_{sat}$ data were within the range of other similar studies and remotely-sensed *chla* errors.

DINEOF is a robust tool enabling a multitude of further applications for satellite datasets, such as construction of spatially continuous fields for biogeochemical or ecosystem modelling (Gregg, 2008), smoothing and noise-reduction, and analyzing phenology and correlations between geophysical variables (McGinty et al., 2016). While all interpolation methods have caveats, the DINEOF method exhibits some major advantages compared to many others (Taylor et al., 2013), which include the minimization of error from iterative processing, utilization of cross-validation data, parameter-free processing and speed of use. For similar datasets to those used here, these

advantages of DINEOF use compared to other spatial interpolation methods can facilitate, for example, further sensitivity testing to more precisely define parameters for each unique dataset and study region (e.g., define ideal percent cross-validation data and covariance filter length). Additionally, DINEOF use is not restricted just to gap-filling or dataset reconstruction, as the EOFs obtained can be used to fill temporal gaps in time series (Kondrashov & Ghil, 2007; Sirjacobs et al., 2011), or even detect noise that can be subtracted to improve dataset quality (e.g., swath-edge error for SSS data (Alvera-Azcárate et al., 2016)).

The findings, discussion, and recommendations raised in this study can assist further work using DINEOF by demonstrating the dependence of outcomes on the input data characteristics. Importantly, the accuracy requirements of a given study and scale of physical processes wishing to be resolved should guide selection of the appropriate input data, in addition to considering the quality and quality-control of input data used. As demonstrated in the sensitivity test, for even low numbers of input scenes (e.g., 100 over a 3-year period), reasonable accuracy ($RMSE_{xval}$) is achievable with DINEOF. Future studies should consider quality-control improvements and gap-filling of a multi-sensor time series to utilize the greatest amount of *chla* for the satellite data record, in addition to improving results through multivariate applications of DINEOF. Further, multivariate DINEOF can increase matchup data available. For the west coast of Canada, further validation of interpolated data can include making use of stationary or continuous *in situ* data acquisition platforms such as buoys and flow-through ship-borne systems, or by accessing local databases of citizen science data. For this region the results of this study

facilitate production of *chla* datasets more effective for studying long-term trends and addressing broader ecological questions, including assisting with fisheries management.

Bibliography

Allen, S. E., & Wolfe, M. A. (2013). Hindcast of the timing of the spring phytoplankton bloom in the Strait of Georgia, 1968-2010. *Progress in Oceanography*, *115*, 6–13. http://doi.org/10.1016/j.pocean.2013.05.026

Alvera-Azcárate, A., Barth, A., Beckers, J. M., & Weisberg, R. H. (2007). Multivariate reconstruction of missing data in sea surface temperature, chlorophyll, and wind satellite fields. *Journal of Geophysical Research: Oceans*, *112*(3), 1–11. http://doi.org/10.1029/2006JC003660

Alvera-Azcárate, A., Barth, A., Parard, G., & Beckers, J. M. (2016). Analysis of SMOS sea surface salinity data using DINEOF. *Remote Sensing of Environment*, *180*, 137–145. http://doi.org/10.1016/j.rse.2016.02.044

Alvera-Azcárate, A., Barth, A., Rixen, M., & Beckers, J. M. (2005). Reconstruction of incomplete oceanographic data sets using empirical orthogonal functions: Application to the Adriatic Sea surface temperature. *Ocean Modelling*, *9*(4), 325–346. http://doi.org/10.1016/j.ocemod.2004.08.001

Alvera-Azcárate, A., Barth, A., Sirjacobs, D., & Beckers, J.-M. (2009). Enhancing temporal correlations in EOF expansions for the reconstruction of missing data using DINEOF. *Ocean Science Discussions*, *6*(2), 1547–1568. http://doi.org/10.5194/osd-6-1547-2009

Alvera-Azcárate, A., Barth, A., Sirjacobs, D., Lenartz, F., & Beckers, J.-M. (2011). Data Interpolating Empirical Orthogonal Functions (DINEOF): a tool for geophysical data analyses. *Medit. Mar. Sci., Special Issue*, 5–11. http://doi.org/10.1029/2006JC003660.J.M.

Alvera-Azcárate, A., Sirjacobs, D., Barth, A., & Beckers, J. M. (2012). Outlier detection in satellite data using spatial coherence. *Remote Sensing of Environment*, *119*, 84–91. http://doi.org/10.1016/j.rse.2011.12.009

Alvera-Azcárate, A., Vanhellemont, Q., Ruddick, K., Barth, A., & Beckers, J. M. (2015). Analysis of high frequency geostationary ocean colour data using DINEOF. *Estuarine, Coastal and Shelf Science*, *159*, 28–36. http://doi.org/10.1016/j.ecss.2015.03.026

Antoine, D., Campbell, J. W., Evans Rsmas, R. H., Gregg, W. W., Lewis, M. R., & Moulin, C. (2004). *IOCCG Report Number 4: Guide to the Creation and Use of Ocean-Colour, Level-3, Binned Data Products*. Retrieved from http://ioccg.org/wp-content/uploads/2015/10/ioccg-report-04.pdf

Bailey, S. W., & Werdell, P. J. (2006). A multi-sensor approach for the on-orbit validation of ocean color satellite data products. *Remote Sensing of Environment*, *102*(1–2),

12–23. http://doi.org/10.1016/j.rse.2006.01.015

Barwell-Clarke, J., & Whitney, F. (1996). *Canadian Technical Report of Hydrography and Ocean Sciences No. 182, Institute of Ocean Sciences Nutrient Methods and Analysis*.

Beckers, J. M., Barth, A., & Alvera-Azcárate, A. (2006). DINEOF reconstruction of clouded images including error maps. Application to the Sea-Surface Temperature around Corsican Island. *Ocean Science Discussions*, *2*(2), 183–199. http://doi.org/10.5194/osd-3-735-2006

Beckers, J. M., Barth, A., Tomazic, I., & Alvera-Azcárate, A. (2014). A method to generate fully multi-scale optimal interpolation by combining efficient single process analyses, illustrated by a DINEOF analysis spiced with a local optimal interpolation. *Ocean Science*, *10*(5), 845–862. http://doi.org/10.5194/os-10-845-2014

Beckers, J. M., & Rixen, M. (2003). EOF calculations and data filling from incomplete oceanographic datasets. *Journal of Atmospheric and Oceanic Technology*, *20*(12), 1839–1856. http://doi.org/10.1175/1520-0426(2003)020<1839:ECADFF>2.0.CO;2

Bennett, A. F. (2002). *Inverse Modeling of the Ocean and Atmosphere* (First Edit). Cambridge, UK: Cambridge University Press.

Blondeau-Patissier, D., Gower, J. F. R., Dekker, A. G., Phinn, S. R., & Brando, V. E. (2014). A review of ocean color remote sensing methods and statistical techniques for the detection, mapping and analysis of phytoplankton blooms in coastal and open oceans. *Progress in Oceanography*, *123*, 123–144. http://doi.org/10.1016/j.pocean.2013.12.008

Brewin, R. J. W., Mélin, F., Sathyendranath, S., Steinmetz, F., Chuprin, A., & Grant, M. (2014). On the temporal consistency of chlorophyll products derived from three ocean-colour sensors. *ISPRS Journal of Photogrammetry and Remote Sensing*, *97*, 171–184. http://doi.org/10.1016/j.isprsjprs.2014.08.013

Campbell, J. W. (1995). The lognormal distribution as a model for bio-optical variability in the se, *100*(C7), 237–254. http://doi.org/10.1029/95JC00458

Carswell, T., Costa, M., Young, E., Komick, N., Gower, J., & Sweeting, R. (2017). Evaluation of MODIS-Aqua Atmospheric Correction and Chlorophyll Products of Western North American Coastal Waters Based on 13 Years of Data. *Remote Sensing*, *9*(10), 1063. http://doi.org/10.3390/rs9101063

Casey, B., Arnone, R., & Flynn, P. (2007). Simple and efficient technique for spatial/temporal composite imagery. *Proceedings of SPIE*, *6680*(668014), 1–8. http://doi.org/10.1117/12.737329

Chittenden, C. M., Beamish, R. J., & McKinley, R. S. (2009). A critical review of Pacific salmon marine research relating to climate. *ICES Journal of Marine Science*, *66*(10), 2195–2204. http://doi.org/10.1093/icesjms/fsp174

Collins, A. K., Allen, S. E., & Pawlowicz, R. (2009). The role of wind in determining the timing of the spring bloom in the Strait of Georgia. *Canadian Journal of Fisheries and Aquatic Sciences*, *66*(9), 1597–1616. http://doi.org/10.1139/F09-071

Corredor-Acosta, A., Morales, C. E., Hormazabal, S., Andrade, I., & Correa-Ramirez, M. A. (2015). Phytoplankton phenology in the coastal upwelling region off central-southern Chile (35S-38S): Time-space variability, coupling to environmental factors, and sources of uncertainty in the estimates. *Journal of Geophysical Research C: Oceans*, *120*, 813–831. http://doi.org/10.1002/2014JC010330

DINEOF - GHER. (n.d.). Retrieved October 1, 2016, from http://modb.oce.ulg.ac.be/mediawiki/index.php/DINEOF

Fisheries and Oceans Canada, Pacific Region, O. S. D. (2018). Institute of Ocean Sciences Data Archive. Retrieved August 28, 2017, from http://www.pac.dfo-mpo.gc.ca/science/oceans/data-donnees/search-recherche/profiles-eng.asp

Ganzedo, U., Alvera-Azcárate, A., Esnaola, G., Ezcurra, A., & Sáenz, J. (2011). Reconstruction of sea surface temperature by means of DINEOF: A case study during the fishing season in the Bay of Biscay. *International Journal of Remote Sensing*, *32*(4), 933–950. http://doi.org/10.1080/01431160903491420

Gregg, W. W. (2008). Assimilation of SeaWiFS ocean chlorophyll data into a three-dimensional global ocean model. *Journal of Marine Systems*, *69*(3–4), 205–225. http://doi.org/10.1016/j.jmarsys.2006.02.015

Gregg, W. W., Bontempi, P., Aiken, J., Gregg, W., Kwiatkowska, E., Mélin, F., … Pinnock, S. (2007). *IOCCG Report 6: Ocean-Colour Data Merging*. *IOCCG*. Retrieved from http://www.ioccg.org

Halverson, M. J., & Pawlowicz, R. (2013). High-resolution observations of chlorophyll-a biomass from an instrumented ferry: Influence of the Fraser River plume from 2003 to 2006. *Continental Shelf Research*, *59*, 52–64. http://doi.org/10.1016/j.csr.2013.04.010

Harrison, P. J., Fulton, J. D., Taylor, F. J. R., & Parsons, T. R. (1983). Review of the Biological Oceanography of the Strait of Georgia: Pelagic Environment. *Canadian Journal of Fisheries and Aquatic Sciences*, *40*(7), 1064–1094. http://doi.org/10.1139/f83-129

Holm-Hansen, O., Lorenzen, C. J., Holmes, R. W., & Strickland, J. D. H. (1965). Fluorometric determination of chlorophyll. *J. Cons. Perm. Int. Explor. Mer.*, *30*, 3–15.

Jackson, J. M., Thomson, R. E., Brown, L. N., Willis, P. G., & Borstad, G. A. (2015). Satellite chlorophyll off the British Columbia Coast, 1997–2010. *Journal of Geophysical Research: Oceans*, *120*(7), 4709–4728. http://doi.org/10.1002/2014JC010496

Johannessen, S. C., Macdonald, R. W., & Paton, D. W. (2003). A sediment and organic carbon budget for the greater Strait of Georgia. *Estuarine, Coastal and Shelf Science*, *56*(3–4), 845–860. http://doi.org/10.1016/S0272-7714(02)00303-7

Jönsson, B. F., & Salisbury, J. E. (2016). Episodicity in phytoplankton dynamics in a coastal region. *Geophysical Research Letters*, *43*, 5821–5828. http://doi.org/10.1002/2016GL068683

Kahru, M., Kudela, R. M., Manzano-Sarabia, M., & Greg Mitchell, B. (2012). Trends in the surface chlorophyll of the California Current: Merging data from multiple ocean color satellites. *Deep-Sea Research Part II: Topical Studies in Oceanography*, *77–80*, 89–98. http://doi.org/10.1016/j.dsr2.2012.04.007

Khangaonkar, T., Long, W., & Xu, W. (2017). Assessment of circulation and inter-basin transport in the Salish Sea including Johnstone Strait and Discovery Islands pathways. *Ocean Modelling*, *109*, 11–32. http://doi.org/10.1016/j.ocemod.2016.11.004

King, M. D., Platnick, S., Menzel, W. P., Ackerman, S. A., & Hubanks, P. A. (2013). Spatial and temporal distribution of clouds observed by MODIS onboard the terra and aqua satellites. *IEEE Transactions on Geoscience and Remote Sensing*, *51*(7), 3826–3852. http://doi.org/10.1109/TGRS.2012.2227333

Komick, N. M. (2007). *Remote Sensing Chlorophyll-a in the Strait of Georgia*. University of Victoria. Retrieved from http://search.proquest.com/docview/20751872?accountid=14656

Komick, N. M., Costa, M. P. F., & Gower, J. (2009). Bio-optical algorithm evaluation for MODIS for western Canada coastal waters: An exploratory approach using in situ reflectance. *Remote Sensing of Environment*, *113*(4), 794–804. http://doi.org/10.1016/j.rse.2008.12.005

Kondrashov, D., & Ghil, M. (2007). Spatio-temporal filling of missing points in geophysical data sets. *Nonlinear Processes in Geophysics*, *14*(1), 3–4. http://doi.org/10.5194/npg-14-3-2007

Land, P., Bailey, T., Taberner, M., Pardo, S., Sathyendranath, S., Nejabati Zenouz, K., … Quartly, G. (2018). A Statistical Modeling Framework for Characterising Uncertainty in Large Datasets: Application to Ocean Colour. *Remote Sensing*, *10*(5), 695. http://doi.org/10.3390/rs10050695

Land, P. E., Shutler, J. D., Platt, T., & Racault, M. F. (2014). A novel method to retrieve oceanic phytoplankton phenology from satellite data in the presence of data gaps. *Ecological Indicators*, *37*, 67–80. http://doi.org/10.1016/j.ecolind.2013.10.008

Li, M., Gargett, A., & Denman, K. (2000). What determines seasonal and interannual variability of phytoplankton and zooplankton in strongly estuarine systems? Application to the semi-enclosed estuary of Strait of Georgia and Juan de Fuca

Strait. *Estuarine, Coastal and Shelf Science*. http://doi.org/10.1006/ecss.2000.0593

Li, Y., & He, R. (2014). Spatial and temporal variability of SST and ocean color in the gulf of maine based on cloud-free SST and chlorophyll reconstructions in 2003-2012. *Remote Sensing of Environment*, *144*, 98–108. http://doi.org/10.1016/j.rse.2014.01.019

Loos, E. A., & Costa, M. (2010). Inherent optical properties and optical mass classification of the waters of the Strait of Georgia, British Columbia, Canada. *Progress in Oceanography*, *87*(1–4), 144–156. http://doi.org/10.1016/j.pocean.2010.09.004

Loos, E., Costa, M., & Johannessen, S. (2017). Underwater optical environment in the coastal waters of British Columbia, Canada. *FACETS*, *2*(2), 872–891. http://doi.org/10.1139/facets-2017-0074

Mackas, D. L., & Harrison, P. J. (1997). Nitrogenous Nutrient Sources and Sinks in the Juan de Fuca Strait/Strait of Georgia/Puget Sound Estuarine System: Assessing the Potential for Eutrophication. *Estuarine, Coastal and Shelf Science*, *44*(1), 1–21. http://doi.org/10.1006/ECSS.1996.0110

Mackas, D. L., Louttit, G. C., & Austin, M. J. (1980). Spatial distribution of zooplankton and phytoplankton in British Columbian coastal waters. *Canadian Journal of Fisheries and Aquatic Sciences*, *37*, 1476–1487.

Marchese, C., Albouy, C., Tremblay, J.-É., Dumont, D., D'Ortenzio, F., Vissault, S., & Bélanger, S. (2017). Changes in phytoplankton bloom phenology over the North Water (NOW) polynya: a response to changing environmental conditions. *Polar Biology*, *40*(9), 1721–1737. http://doi.org/10.1007/s00300-017-2095-2

Mass, C., Johnson, N., Warner, M., & Vargas, R. (2015). Synoptic Control of Cross-Barrier Precipitation Ratios for the Cascade Mountains. *Journal of Hydrometeorology*, *16*(3), 1014–1028. http://doi.org/10.1175/JHM-D-14-0149.1

Masson, D. (2006). Seasonal water mass analysis for the straits of Juan de fuca and Georgia. *Atmosphere-Ocean*, *44*(1), 1–15. http://doi.org/10.3137/ao.440101

Masson, D., & Peña, A. (2009). Chlorophyll distribution in a temperate estuary: The Strait of Georgia and Juan de Fuca Strait. *Estuarine, Coastal and Shelf Science*, *82*(1), 19–28. http://doi.org/10.1016/j.ecss.2008.12.022

Masson, D., & Perry, R. I. (2013). The strait of georgia ecosystem research initiative: An overview. *Progress in Oceanography*, *115*, 1–5. http://doi.org/10.1016/j.pocean.2013.05.009

Mauri, E., Poulain, P.-M., & Notarstefano, G. (2008). Spatial and temporal variability of the sea surface temperature in the Gulf of Trieste between January 2000 and December 2006. *Journal of Geophysical Research*, *113*(C10), C10012. http://doi.org/10.1029/2007JC004537

Mauri, E., Poulain, P. M., & Južnič-Zonta, Ž. (2007). MODIS chlorophyll variability in the northern Adriatic Sea and relationship with forcing parameters. *Journal of Geophysical Research: Oceans*, *112*(3), 1–14. http://doi.org/10.1029/2006JC003545

McGinty, N., Guðmundsson, K., Ágústsdóttir, K., & Marteinsdóttir, G. (2016). Environmental and climactic effects of chlorophyll-a variability around Iceland using reconstructed satellite data fields. *Journal of Marine Systems*, *163*, 31–42. http://doi.org/10.1016/j.jmarsys.2016.06.005

Meister, G., & McClain, C. R. (2010). Point-spread function of the ocean color bands of the Moderate Resolution Imaging Spectroradiometer on Aqua. *Applied Optics*, *49*, 6276–6285. http://doi.org/10.1364/AO.49.006276

Meister, G., Zong, Y., & McClain, C. R. (2008). Derivation of the MODIS Aqua Point-Spread Function for Ocean Color Bands. *Proceedings of SPIE*, *7081*(V0811F), 70811F–1–70811F–12. http://doi.org/10.1117/12.796980

Mélin, F., Vantrepotte, V., Chuprin, A., Grant, M., Jackson, T., & Sathyendranath, S. (2017). Assessing the fitness-for-purpose of satellite multi-mission ocean color climate data records: A protocol applied to OC-CCI chlorophyll-a data. *Remote Sensing of Environment*. http://doi.org/10.1016/j.rse.2017.03.039

Miles, T. N., He, R., & Li, M. (2009). Characterizing the South Atlantic Bight seasonal variability and cold-water event in 2003 using a daily cloud-free SST and chlorophyll analysis. *Geophysical Research Letters*, *36*(2), 1–6. http://doi.org/10.1029/2008GL036396

Müller, D. (2007). Estimation of algae concentration in cloud covered scenes using geostatistical methods. In *Proc. "Envisat Symposium 2007"* (pp. 23–27). Montreux, Switzerland.

NASA Ocean Color. (n.d.). Retrieved September 1, 2015, from https://oceancolor.gsfc.nasa.gov/

NASA SeaDAS. (n.d.). Retrieved September 1, 2015, from https://seadas.gsfc.nasa.gov/

Nechad, B., Alvera-Azcárate, A., Ruddick, K., & Greenwood, N. (2011). Reconstruction of MODIS total suspended matter time series maps by DINEOF and validation with autonomous platform data. *Ocean Dynamics*, *61*(8), 1205–1214. http://doi.org/10.1007/s10236-011-0425-4

O'Reilly, J. E., Maritorena, S., Siegel, D. A., O'Brien, M. C., Toole, D., Mitchell, B. G., … Culver, M. (2000). *Ocean color chlorophyll a algorithms for SeaWiFS, OC2, and OC4: version 4. In SeaWiFS Postlaunch Calibration and Validation Analyses, Part 3, NASA Tech. Memo. 2000-206892, 11*. Greenbelt, MD.

Peña, A., Masson, D., & Callendar, W. (2016). Annual plankton dynamics in a coupled physical-biological model of the Strait of Georgia, British Columbia. *Progress in*

Oceanography, *146*, 58–74.

Perry, R. I. (1984). *Plankton Blooms of the British Columbia Northern Shelf: Seasonal Distributions and Mechanisms Influencing their Formation*. University of British Columbia. Retrieved from http://search.proquest.com/docview/303365535?accountid=14656

Phillips, S. R., & Costa, M. (2017). Spatial-temporal bio-optical classification of dynamic semi-estuarine waters in western North America. *Estuarine, Coastal and Shelf Science*, *199*, 35–48. http://doi.org/10.1016/j.ecss.2017.09.029

Porter, A. D., Rechisky, E. L., Winchell, P., & Welch, D. W. (2016). The Use of Telemetry to Investigate Residence Time and Survival of Fraser River Chinook Salmon in the Strait of Georgia, 2016. Salish Sea Marine Survival Project.

Ruddick, K. G., Ovidio, F., & Rijkeboer, M. (2000). Atmospheric correction of SeaWiFS imagery for turbid coastal and inland waters. *Applied Optics*, *39*(6), 897. http://doi.org/10.1364/AO.39.000897

Sathyendranath, S., Brewin, R. J. W., Jackson, T., Mélin, F., & Platt, T. (2017). Ocean-colour products for climate-change studies: What are their ideal characteristics? *Remote Sensing of Environment*, *203*, 125–138. http://doi.org/10.1016/j.rse.2017.04.017

Sherwood, S. (2000). Climatic signals from station arrays with missing data, and an application to winds. *Journal of Geophysical Research*, *105*, 29489–29500.

Sirjacobs, D., Alvera-Azcárate, A., Barth, A., Lacroix, G., Park, Y., Nechad, B., … Beckers, J. M. (2011). Cloud filling of ocean colour and sea surface temperature remote sensing products over the Southern North Sea by the Data Interpolating Empirical Orthogonal Functions methodology. *Journal of Sea Research*, *65*(1), 114–130. http://doi.org/10.1016/j.seares.2010.08.002

Smith, T. M., Reynolds, R. W., Levezey, R. E., & Stokes, D. C. (1996). Reconstruction of historical sea surface temperatures using empirical orthogonal functions. *Journal of Climate*, *9*, 1403–1420.

Strang, G. (1988). *Linear Algebra and Its Applications* (Third Edit). Harcourt-Brace-Jovanovich.

Taylor, M. H., Losch, M., Wenzel, M., & Schröter, J. (2013). On the sensitivity of field reconstruction and prediction using empirical orthogonal functions derived from Gappy data. *Journal of Climate*, *26*(22), 9194–9205. http://doi.org/10.1175/JCLI-D-13-00089.1

Waite, J. N., & Mueter, F. J. (2013). Spatial and temporal variability of chlorophyll-a concentrations in the coastal Gulf of Alaska, 1998-2011, using cloud-free reconstructions of SeaWiFS and MODIS-Aqua data. *Progress in Oceanography*,

116, 179–192. http://doi.org/10.1016/j.pocean.2013.07.006

Wang, M. (2007). Remote sensing of the ocean contributions from ultraviolet to near-infrared using the shortwave infrared bands: simulations. *Applied Optics*, *46*(9), 1535. http://doi.org/10.1364/AO.46.001535

Wang, Y., Jiang, H., Jin, J., Zhang, X., Lu, X., & Wang, Y. (2015). Spatial-Temporal Variations of Chlorophyll-a in the Adjacent Sea Area of the Yangtze River Estuary Influenced by Yangtze River Discharge. *International Journal of Environmental Research and Public Health*, *12*(5), 5420–5438. http://doi.org/10.3390/ijerph120505420

Wang, Y., & Liu, D. (2014). Reconstruction of satellite chlorophyll-a data using a modified DINEOF method: A case study in the Bohai and Yellow seas, China. *International Journal of Remote Sensing*, *35*(1), 204–217. http://doi.org/10.1080/01431161.2013.866290

Ware, D. M., & Thomson, R. E. (2005). Bottom-up Ecosystem Trophic Dynamics Determine Fish Production in the Northeast Pacific. *Science*, *308*(5726), 1280–1284. Retrieved from http://www.jstor.org

Werdell, P. J., Bailey, S. W., Franz, B. A., Harding, L. W., Feldman, G. C., & McClain, C. R. (2009). Regional and seasonal variability of chlorophyll-a in Chesapeake Bay as observed by SeaWiFS and MODIS-Aqua. *Remote Sensing of Environment*, *113*(6), 1319–1330. http://doi.org/10.1016/J.RSE.2009.02.012

Wilks, D. S. (2006). *Statistical Methods in the Atmospheric Sciences*. *Meteorological Applications* (Second Edi). London: Academic Press. http://doi.org/10.1016/B978-0-12-385022-5.00008-7

Yin, K., Goldblatt, R. H., Harrison, P. J., St. John, M. A., Clifford, P. J., & Beamish, R. J. (1997). Importance of wind and river discharge in influencing nutrient dynamics and phytoplankton production in summer in the central Strait of Georgia. *Marine Ecology Progress Series*, *161*, 173–183. http://doi.org/10.3354/meps161173

Appendix A:
Explained variance of EOF modes for each trial

Table 4. Percent explained variance and cumulative variance calculated for each input dataset

(a)	Explained Variance (%)				Cumulative Variance (%)			
EOF	**$D1_{2014}$**	**$D1_{2015}$**	**$D1_{2016}$**	**D3**	**$D1_{2014}$**	**$D1_{2015}$**	**$D1_{2016}$**	**D3**
1	35.76	45.14	37.21	35.14	35.76	45.14	37.21	35.14
2	21.56	19.44	28.90	17.38	57.32	64.58	66.11	52.52
3	7.45	9.11	8.40	7.99	64.77	73.69	74.51	60.51
4	7.00	5.19	5.56	6.20	71.77	78.88	80.07	66.71
5	5.47	4.94	4.62	4.40	77.24	83.82	84.69	71.11
6	3.84	4.02	3.23	3.12	81.08	87.84	87.92	74.23
7	3.82	3.10	2.70	2.96	84.90	90.94	90.62	77.19
8	3.59	2.82	2.64	2.10	88.49	93.76	93.26	79.29
9	3.05	2.56	1.81	1.61	91.54	96.32	95.07	80.90
10	2.56			1.53	94.10			82.43
11	1.94			1.52	96.04			83.95
12				1.47				85.42
13				1.32				86.74
14				1.21				87.95
15				1.03				88.98
16				1.02				90.00
17				1.01				91.01
18				0.87				91.88
19				0.85				92.73
20				0.82				93.55
21				0.74				94.29
22				0.70				94.99
23				0.64				95.63
24				0.58				96.21
25				0.47				96.68
26				0.47				97.08

(b)

EOF	**$W1_{2014}$**	**$W1_{2015}$**	**$W1_{2016}$**	**W3**	**$W1_{2014}$**	**$W1_{2015}$**	**$W1_{2016}$**	**W3**
1	31.57	30.54	31.20	26.36	31.57	30.54	31.20	26.36
2	25.46	30.02	25.69	23.04	57.03	60.56	56.89	49.40
3	11.96	14.13	16.62	7.63	68.99	74.69	73.51	57.03
4				7.28				64.31
5				3.96				68.27
6				3.71				71.98
7				2.45				74.43
8				2.45				76.88

Appendix B:
Median *chla* Time Series

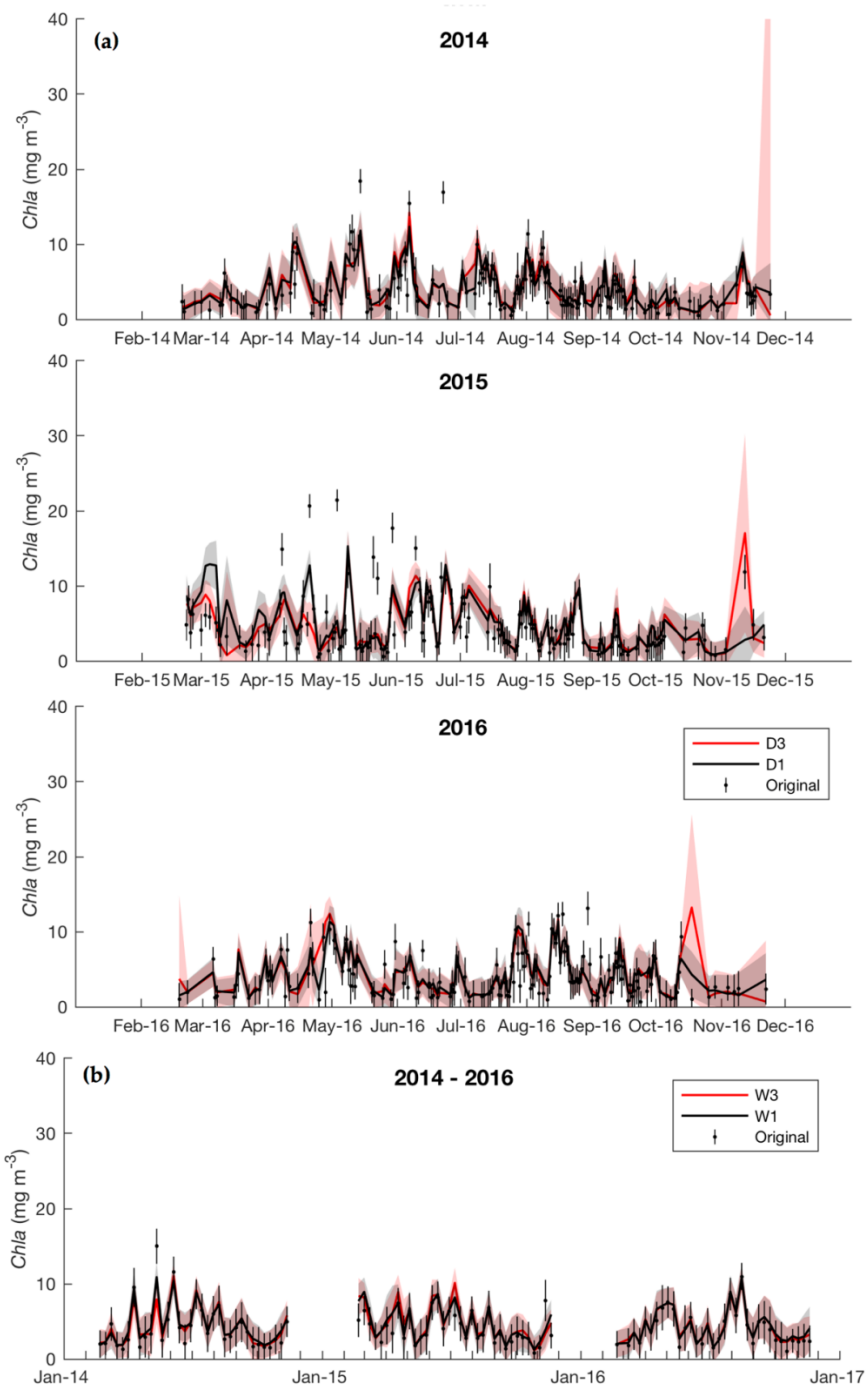

Figure 13. Spatial median and shaded ±1 standard deviation for $chla_{sat+rec}$ of D1 / D3 (a), divided by year for legibility, and 2014 - 2016 for W1 / W3 (b). Corresponding per-scene median $chla_{sat}$ shown as black dots with ±1 standard deviation.